2008

The relations among 8, 24 and 160 mu m dust emission within nearby spiral galaxies

GJ Bendo

BT Draine

CW Engelbracht

G Helou

MD Thornley

See next page for additional authors

Recommended Citation

Bendo, GJ; Draine, BT; Engelbracht, CW; Helou, G; Thornley, MD; Bot, C; Buckalew, BA; Calzetti, D; Dale, DA; Hollenbach, J; Li, A; and Moustakas, J, "The relations among 8, 24 and 160 mu m dust emission within nearby spiral galaxies" (2008). *MONTHLY NOTICES OF THE ROYAL ASTRONOMICAL SOCIETY*. 142.
https://doi.org/10.1111/j.1365-2966.2008.13567.x

Mon. Not. R. Astron. Soc. 000, 1–24 () Printed 17 June 2008 (MN LATEX style file v2.2)

The relations among 8, 24, and 160 μm dust emission within nearby spiral galaxies

G. J. Bendo[1], B. T. Draine[2], C. W. Engelbracht[3], G. Helou[4], M. D. Thornley[5], C. Bot[6], B. A. Buckalew[7], D. Calzetti[8], D. A. Dale[9], D. J. Hollenbach[10], A. Li[11], J. Moustakas[12]

[1]Astrophysics Group, Imperial College, Blackett Laboratory, Prince Consort Road, London SW7 2AZ, United Kingdom
[2]Princeton University Observatory, Peyton Hall, Princeton, NJ 08544-1001, USA
[3]Steward Observatory, University of Arizona, 933 North Cherry Avenue, Tucson, AZ 85721, USA
[4]California Institute of Technology, MC 314-6, Pasadena, CA 91101, USA
[5]Department of Physics & Astronomy, Bucknell University, Lewisburg, PA 17837, USA
[6]Spitzer Science Center, California Institute of Technology, MS 220-6, Pasadena, CA 91101, USA
[7]Department of Physics, Embry-Riddle Aeronautical University, 3700 Willow Creek Road, Prescott, AZ 86301, USA
[8]Department of Astronomy, University of Massachusetts, LGRT-B 254, 710 North Pleasant Street, Amherst, MA 01002, USA
[9]Department of Physics and Astronomy, University of Wyoming, Laramie, WY 82071, USA
[10]NASA Ames Research Center, MS 245-3, Moffett Field, CA 94035-1000, USA
[11]Department of Physics and Astronomy, University of Missouri, Columbia, MO 65211, USA
[12]Department of Physics, New York University, 4 Washington Place, New York, NY 10003, USA

ABSTRACT

We investigate the relations among the stellar continuum-subtracted 8 μm polycyclic aromatic hydrocarbon (PAH 8 μm) emission, 24 μm hot dust emission, and 160 μm cold dust emission in fifteen nearby face-on spiral galaxies in the Spitzer Infrared Nearby Galaxies Survey sample. The relation between PAH 8 and 24 μm emission measured in $\sim$ 2 kpc regions is found to exhibit a significant amount of scatter, and strong spatial variations are observed in the (PAH 8 μm)/24 μm surface brightness ratio. In particular, the (PAH 8 μm)/24 μm surface brightness ratio is observed to be high in the diffuse interstellar medium and low in bright star-forming regions and other locations with high 24 μm surface brightness. PAH 8 μm emission is found to be well-correlated with 160 μm emission on spatial scales of $\sim$ 2 kpc, and the (PAH 8 μm)/160 μm surface brightness ratio is generally observed to increase as the 160 μm surface brightness increases. These results suggest that the PAHs are associated with the diffuse, cold dust that produces most of the 160 μm emission in these galaxies, and the variations in the (PAH 8 μm)/160 μm ratio may generally be indicative of either the intensity or the spectrum of the interstellar radiation field that is heating both the PAHs and the diffuse interstellar dust.

Key words: galaxies: ISM, infrared: galaxies

1 INTRODUCTION

Observations of nearby spiral galaxies with the Infrared Space Observatory (ISO) demonstrated that polycyclic aromatic hydrocarbon (PAH) spectral feature emission at $\sim$ 8 μm is closely associated with hot dust emission at 15 μm, and the 8 μm emission was also shown to be correlated with other star formation tracers (Roussel et al. 2001; Förster Schreiber et al. 2004). However, observations with the Spitzer Space Telescope (Werner et al. 2004) have demonstrated that the correlation of PAH emission at 8 μm to hot dust emission at 24 μm was not necessarily a one-to-one correlation within individual galaxies. Helou et al. (2004), Bendo et al. (2006), and Gordon et al. (2008) demonstrated that, on scales of hundreds of parsecs, continuum-subtracted PAH emission at 8 μm (henceforth referred to as PAH 8 μm emission) does not accurately trace 24 μm emission. In particular, PAH 8 μm emission seems to appear in shell-like features around star-forming regions, while 24 μm emission peaks within star-forming regions. Using images of M51, Calzetti et al. (2005) demonstrated that PAH 8 μm emission compared to other tracers of star formation, including 24 μm emission, is disproportionately low within star-forming regions and disproportionately high in

diffuse regions. The results from Calzetti et al. (2007) show that the PAH 8 μm/24 μm emission ratio measured in HII regions is partly dependent on the aperture used for measuring the flux densities, which also suggest that a significant fraction of PAH 8 μm emission originates from outside the HII regions. Thilker et al. (2007) also demonstrated that the PAH 8 μm/24 μm ratio of HII regions in NGC 7331 may depend on infrared, Hα, or ultraviolet surface brightness after corrections for dust extinction have been applied, which implied that PAH 8 μm emission is suppressed within strong star-forming regions. Engelbracht et al. (2005), Dale et al. (2005), Draine et al. (2007), and Engelbracht et al. (2008) have demonstrated that the global 8 μm/24 μm emission ratio may decrease in regions with lower metallicity, and Calzetti et al. (2007) also demonstrated that this ratio for HII regions in other galaxies depends on metallicity. Although these studies based on Spitzer data have shown explicitly or implicitly that the relation between 8 μm PAH emission and 24 μm emission on $\lesssim$1 kpc scales is not a one-to-one relation, no study has yet explored variation in the (PAH 8 μm)/24 μm ratio between diffuse and star-forming regions within a broad range of spiral galaxies.

While most research has focused on comparisons between PAH emission and hot dust emission, some additional studies have compared PAH emission to cold dust emission at wavelengths longer than 100 μm. Using ISO data, Mattila et al. (1999) and Haas et al. (2002) demonstrated that PAH emission at 8 μm is correlated with large grain emission, and Haas et al. (2002) even argued that the correlation between 8 μm emission and cold dust emission at 850 μm was much stronger than the correlation between 8 and 15 μm emission. Using Spitzer data, Bendo et al. (2006) demonstrated that PAH 8 μm emission was correlated with 160 μm cold dust emission in NGC 4631, but the ratio of (PAH 8 μm)/160 μm emission varied. Although the (PAH 8 μm)/160 μm ratio appeared related to the infrared surface brightness in NGC 4631, Bendo et al. (2006) used bright infrared sources in the outer disc to argue that the variations in the (PAH 8 μm)/160 μm ratio are instead dependent on radius. Given that the ratio of PAH emission to dust emission at longer wavelengths or the ratio of PAHs to total dust mass may vary with metallicity (Engelbracht et al. 2005; Dale et al. 2005; Smith et al. 2007; Draine et al. 2007; Engelbracht et al. 2008) and that metallicity is generally expected to vary with radius within spiral galaxies (e.g. Searle 1971; Webster & Smith 1983; Vila-Costas & Edmunds 1992; Zaritsky et al. 1994; van Zee et al. 1998; Pilyugin et al. 2004, J. Moustakas et al. 2008, in preparation), the results from NGC 4631 suggested that the variations in (PAH 8 μm)/160 μm ratio within that galaxy could be related to metallicity. Unfortunately, NGC 4631 is viewed edge-on, so local variations in the observed (PAH 8 μm)/160 μm ratio that are not dependent on radius may be suppressed by the line-of-sight integrations through the disc. Variations in the (PAH 8 μm)/160 μm ratio and its dependence on both infrared surface brightness and radius need to be studied further using spiral galaxies with orientations closer to face-on.

In this paper, we examine the relation of PAH 8 μm emission to both 24 μm hot dust emission and 160 μm cold dust emission in a set of fifteen face-on spiral galaxies observed by Spitzer as part of the Spitzer Infrared Nearby Galaxies Survey (SINGS) legacy project (Kennicutt et al. 2003). The basic goal is to understand how PAH 8 μm emission is related to dust emission at other wavelengths. Section 2 provides basic information on the wave bands used in the analysis, the observations and data reductions, the sample, and the preparation of the data for the analysis. The comparison between PAH 8 and 24 μm emission is presented in Section 3, and the comparison between PAH 8 and 160 μm emission is presented in Section 4. The analysis is then followed by a discussion in Section 5 and conclusions in Section 6.

2 DATA

2.1 Wave band information

Here we present background information on the 8 μm, 24 μm, and 160 μm bands used for the analysis in this paper. This information also includes some caveats that should be considered when interpreting the results from these data.

Channel 4 of the Infrared Array Camera (IRAC; Fazio et al. 2004) covers a region centered on 8.0 μm that includes the 7.7 μm PAH feature as well as some stellar continuum and some hot dust emission (e.g. Smith et al. 2007). For the analysis here, the stellar continuum is subtracted using 3.6 μm data from channel 1 of IRAC. Although the PAH emission features are very prominent in this 8 μm band, thermal emission from larger grains may contribute significantly to emission in this band in regions with very intense radiation fields (Draine & Li 2007).

The 24 μm detector of the Multiband Imaging Photometer for Spitzer (MIPS; Rieke et al. 2004) mostly detects hot ($\gtrsim$100 K) dust emission within nearby galaxies. In environments with low radiation fields, this dust emission may originate from mostly transiently-heated small grains, but in regions with high radiations fields such as star-forming regions, the emission consists of mostly thermal emission from grains at equilibrium temperatures of $\gtrsim$100 K (e.g. Li & Draine 2001; Draine & Li 2007). The relative contribution of dust at $\gtrsim$100 K is expected to be strongly dependent on the strength of the illuminating radiation field. Consequently, the 24 μm band is predicted to increase more rapidly than other infrared bands as the illuminating radiation field increases, as has been shown with many physical and semi-empirical models of dust emission (e.g. Dale et al. 2001; Li & Draine 2001; Draine & Li 2007). Multiple studies with Spitzer data have shown that the 24 μm emission from point-like sources corresponds to HII regions visible in optical and ultraviolet wave bands, so the 24 μm band may be used to measure star formation activity (Prescott et al. 2007; Calzetti et al. 2007). Extended 24 μm emission, however, may originate from outside of star-forming regions in the diffuse interstellar medium.

The 160 μm MIPS detector mainly traces cold ($\sim$ 20 K) dust emission that may be associated with cirrus dust in the diffuse interstellar medium (e.g. Draine et al. 2007). Because the 160 μm band samples dust emission near the peak of the spectral energy distribution in the galaxies in this sample (Dale et al. 2005), the 160 μm band should be tightly correlated with the total infrared (TIR) luminosity. This is explained in the following proof. For thermal emission mod-

ified by an emissivity function that scales as ν^{β}, the total energy emitted in a single wave band (νL_{ν}) should scale as

$$\nu L_{\nu} \propto \frac{\nu^{(4+\beta)}}{e^{x}-1} \quad (1)$$

where

$$x = \frac{h\nu}{kT}. \quad (2)$$

The total integrated thermal emission L_{total} will scale according to

$$L_{total} \propto T^{(4+\beta)}. \quad (3)$$

The ratio of νL_{ν} to L_{total} will be approximately constant (e.g. independent of grain temperature) when it is close to a maximum, which occurs when

$$\frac{xe^{x}}{e^{x}-1} = 4+\beta. \quad (4)$$

Since $e^{x} >> 1$, then

$$T \approx \frac{1}{4+\beta}\frac{h\nu}{k}. \quad (5)$$

Assuming that β equals 2 (Li & Draine 2001), this condition is met at 160 μm when the dust temperature is $\sim$ 15 K. Because the peak of the spectral energy distribution is actually at a shorter wavelength than 160 μm, the ratio of 160 μm emission to total infrared emission should decrease slightly as the illuminating radiation field increases.

2.2 Observations and data reduction

We use the 3.6, 8.0, 24, 70, and 160 μm data taken with Spitzer as part of SINGS. The 3.6 and 8.0 μm observations were performed with IRAC. The observations for each object consisted of a series of 5 arcmin $\times$ 5 arcmin individual frames taken in either a mosaic or a single field dither pattern. The 24, 70, and 160 μm observations performed with MIPS are composed of two scan maps for each target. Each object was observed twice in each wave band to identify and remove transient phenomena, particularly asteroids. The full-width half-maxima (FWHM) of the point spread functions (PSFs), as stated in the Spitzer Observer's Manual (Spitzer Science Center 2006)[6], are 1.7, 2.0, 6, and 38 arcsec at 3.6, 8.0, 24, and 160 μm, respectively. Details on the observations can be found in the documentation for the SINGS fourth data delivery (SINGS Team 2006)[7].

The IRAC data were processed using the SINGS IRAC pipeline, which combines multiple frames of data using a drizzle technique. A description of the technique is presented in Regan et al. (2006). The final images may contain residual background emission from the telescope or sky that is subtracted during the analysis. The MIPS data were processed using the MIPS Data Analysis Tools version 3.06 (Gordon et al. 2005). Additional software was used to remove zodiacal light emission and improve the flatfielding in the 24 μm data and to remove short-term variations in the background signal (commonly referred to as drift) in the 70 and 160 μm data. Any additional background offset left in the final images was measured in regions outside the optical discs and subtracted. Additional details are presented in Bendo et al. (2006). Full details on the data processing are also available in the SINGS documentation for the fourth data delivery (SINGS Team 2006).

2.3 Sample selection

To perform this analysis, we need to resolve substructures in the 160 μm images, which have PSFs with FWHM of 38 arcsec. We therefore limit the sample to spiral galaxies in SINGS where the major axes of the D_{25} isophote specified by de Vaucouleurs et al. (1991) are larger than 5 arcmin. Since we want to be able to distinguish between radial colour variations and colour variations related to the presence of substructures and since such substructures are difficult to study in edge-on galaxies, we only use galaxies that are inclined less than $\sim$ 60 deg. The inclinations are calculated using

$$i = \cos^{-1}\left(\sqrt{\frac{q^{2}-q_{o}^{2}}{1-q_{o}^{2}}}\right). \quad (6)$$

The value q is the observed (projected) minor-to-major axis ratio. The value q_o is the intrinsic optical axial ratio (the ratio of the unprojected optical axis perpendicular the plane of the galaxy to the diameter of the disc), which is equivalent to 0.20 for most disc galaxies (Tully 1998). Because the optical disc of NGC 5194 may be distorted by its interaction with NGC 5195, its inclination is not calculated using this equation. Instead, the inclination as well as the position angle given by García-Gómez et al. (2002) are used for the analysis.

Six of the SINGS galaxies that meet the above criteria are unsuitable for the analysis. NGC 1512 and NGC 4826 are not used because only the central regions were detected at the 5σ levels in all of the convolved maps (described in the next section). The 8.0 μm images of NGC 1097, NGC 1566, and NGC 4736 are heavily affected by muxbleed artefacts (artificially bright columns of pixels associated with high-surface brightness sources) that cross over significant fractions of the optical discs, so those data are not usable for this analysis. Two very bright foreground stars in the 3.6 and 8.0 μm images of NGC 3621 cause problems in the analysis, so NGC 3621 needs to be excluded from the sample as well. The other 15 galaxies that meet the above criteria, which are roughly uniformly distributed between Hubble types Sab and Sd, are listed in Table 1 along with information on the galaxies' morphologies, optical axes, distances, nuclear spectral types, and nebular oxygen abundances (12+log(O/H), which is treated as representative of the global metallicities of the galaxies).

2.4 Data preparation

Many Spitzer studies of infrared colour variations within individual galaxies have relied on flux densities measured within discrete subregions that are chosen either by eye or by source identification software. However, this selection process may be biased. Some subregions within the galaxy might be excluded from the analysis, especially if the regions are selected by eye, and region selection may also be biased towards regions that appear bright in a specific wave

[6] http://ssc.spitzer.caltech.edu/documents/som/
[7] Available at http://ssc.spitzer.caltech.edu/legacy/singshistory.html

Table 1. Basic Properties of the Sample Galaxies

Name	Hubble Type[a]	Size of Optical Disc (arcmin)[a]	Inclination[b] Angle[c]	Position (Mpc)[d]	Distance	Distance Reference[e]	Nuclear Type[f]	12+log(O/H)[g]
NGC 628	SA(s)c	10.5×9.5	26°	25°	7.3 ± 1.4	1	SF	8.33 ± 0.02
NGC 925	SAB(s)d	10.5×5.9	58°	102°	9.12 ± 0.17	2	SF	8.24 ± 0.01
NGC 2403	SAB(s)cd	21.9×12.3	58°	127°	3.13 ± 0.14	2	SF	8.31 ± 0.01
NGC 3031	SA(s)ab	26.9×14.1	60°	157°	3.55 ± 0.15	2	AGN	8.40 ± 0.01
NGC 3184	SAB(rs)cd	7.4×6.9	22°	135°	11.1 ± 1.9	3	SF	8.48 ± 0.02
NGC 3351	SB(r)b	7.4×5.0	49°	13°	9.3 ± 0.4	2	SF	8.61 ± 0.01
NGC 3938	SA(s)c	5.4×4.9	25°	42°∗	13.4 ± 2.3	4	SF	8.44 ± 0.18
NGC 4254	SA(s)c	5.4×4.7	30°	68°∗	16.5 ± 0.6	5	SF	8.46 ± 0.02
NGC 4321	SAB(s)bc	7.4×6.3	32°	30°	14.3 ± 0.5	2	AGN	8.50 ± 0.04
NGC 4579	SAB(rs)b	5.9×4.7	38°	95°	16.5 ± 0.6	5	AGN	8.55 ± 0.18
NGC 4725	SAB(r)ab pec	10.7×7.6	46°	35°	11.9 ± 0.3	2	AGN	8.40 ± 0.05
NGC 5055	SA(rs)bc	12.6×7.2	57°	105°	7.8 ± 2.3	4	AGN	8.42 ± 0.04
NGC 5194	SA(s)bc pec	11.2×6.9	20°	170°	8.4 ± 0.6	6	AGN	8.54 ± 0.01
NGC 6946	SAB(rs)cd	11.5×9.8	32°	80°∗	6.8 ± 1.7	7	SF	8.40 ± 0.04
NGC 7793	SA(s)d	9.3×6.3	49°	98°	3.9 ± 0.4	8	SF	8.27 ± 0.03

[a] These data are taken from de Vaucouleurs et al. (1991). The optical disc is the size of the D_{25} isophote.
[b] The inclinations are calculated using the dimensions of the galaxies and Equation 6. An exception is made for NGC 5194, where the inclination from García-Gómez et al. (2002) was used.
[c] The position angles are measured in degrees from north through east. These data are taken from de Vaucouleurs et al. (1991) when given. The position angle for NGC 5194 was taken from García-Gómez et al. (2002). Position angles marked with an asterisk are measured in the 3.6 μm data using the IDL fit_ellipse program by D. Fanning (accessible from http://www.dfanning.com/documents/programs.html). These position angles have uncertainties of $\sim 5°$.
[d] These distances are part of a compilation of distance for the complete SINGS sample will be presented in J. Moustakas et al. (2008, in preparation).
[e] Distance references - (1) Sharina et al. (1996); (2) Freedman et al. (2001); (3) Leonard et al. (2002); (4) Masters (2005); (5) Mei et al. (2007); (6) Feldmeier et al. (1997); (7) Karachentsev et al. (2000); (8) Karachentsev et al. (2003).
[f] The nucleus types are based on the analysis of the optical spectrophotometric properties by J. Moustakas et al. (2008, in preparation). The spectral type indicates whether the center of each object is dominated by star formation (SF) or an active galactic nucleus (AGN). See J. Moustakas et al. (2008, in preparation) for more details.
[g] These are the characteristic nebular oxygen abundances presented by J. Moustakas et al. (2008, in preparation) using the Pilyugin & Thuan (2005) strong-line calibration. They are representative of the mean, luminosity-weighted oxygen abundance of each galaxy. Note that the uncertainties only include statistical measurement errors, and do not include any systematic uncertainties in the adopted abundance scale (see J. Moustakas et al. 2008, in preparation for more details). Although J. Moustakas et al. also present abundances based on the Kobulnicky & Kewley (2004) strong-line calibration, we adopt the abundances based on the Pilyugin & Thuan (2005) calibration because they are comparable to the abundances used by Engelbracht et al. (2008).

band. To avoid this bias, we divide each galaxy into 45 arcsec square regions and extract surface brightnesses for all usable regions within the optical discs of the galaxies. This approach samples the whole of the galactic disc and avoids any subjective biases. We choose to use 45 arcsec regions because it is an integer multiple of the pixels used in the original images, and it is larger than the 38 arcsec FWHM of the 160 μm images. Note that 45 arcsec corresponds to physical scales of $\sim$ 0.7-3.6 kpc for the galaxies in this sample.

First, the data are convolved with kernels that match the PSFs of the images in the 3.6, 8, 24, and 70 μm bands to the PSF of the 160 μm data, which has a FWHM of 38 arcsec. The convolution kernels were created by (Gordon et al. 2008) using the ratio of the Fourier transforms of the input and output PSFs, with high-frequency noise suppressed in the input PSFs[8]. By doing this, it is possible to directly compare surface brightnesses measured in the same apertures in different wave bands without applying any aperture corrections. Next, the coordinate systems across all the wave bands are matched to each other using point-like sources (stars, background galaxies, or infrared-bright regions within the galaxies) or the centres of the galaxies as guides. The background in the IRAC data was then subtracted from the images. Following this, the data are rebinned into 45 arcsec square regions such that the coordinates of the rebinned pixels match across all wave bands. Because the centres of the galaxies are mapped into the corners of four pixels in the MIPS images, the centres of the galaxies fall at the corners of four 45 arcsec bins. We then extract surface brightnesses from all 45 arcsec regions within the optical discs of the galaxies. We exclude from the analysis regions not detected at the 3σ level in one or more wave bands, regions contaminated by emission from bright foreground stars (identified as unresolved sources in the unconvolved IRAC data with 3.6 μm/8 μm surface brightness ratios $\gtrsim$5), and regions affected by muxbleed at 8 μm. Additionally, we exclude the centre of NGC 5195 from the analysis of NGC 5194 because the dwarf galaxy causes confusion when interpreting the data on the spiral galaxy. To correct for the diffusion of light through the IRAC detector substrate, the 3.6 and 8.0 μm data are multiplied by the "infinite" aperture corrections described by Reach et al. (2005) (which should not

[8] The kernels are available at http://dirty.as.arizona.edu/∼kgordon/mips/conv_psfs/conv_psfs.html.

Table 2. Uncertainties in the Surface Brightness Ratios Related to Matching Image Coordinate Systems

Surface Brightness Ratio	Uncertainty
I_ν(PAH 8 μm)/I_ν(24 μm)	0.005
I_ν(PAH 8 μm)/I_ν(160 μm)	0.0015
νI_ν(PAH 8 μm)/I(TIR)	0.007
$I\nu$(24 μm)/I_ν(160 μm)	0.005
νI_ν(160 μm)/I(TIR)	0.02

be confused with the types of aperture corrections used for measuring the flux densities of unresolved sources). The correction factors are 0.944 and 0.737 at 3.6 and 8.0 μm, respectively. Finally, we subtract the stellar continuum from the 8 and 24 μm surface brightnesses (in MJy sr^{-1}) using

$$I_\nu(PAH\ 8\mu m) = I_\nu(8\mu m) - 0.232 I_\nu(3.6\mu m) \quad (7)$$

$$I_\nu(24\mu m) = I_\nu(24\mu m) - 0.032 I_\nu(3.6\mu m), \quad (8)$$

which were derived by Helou et al. (2004). For the galaxies in this analysis, this is a correction of $\sim$ 1 %-4% to the 24 μm surface brightnesses but a correction of $\sim$ 5%-25% to the 8 μm surface brightnesses. The stellar continuum-subtracted 8 μm data are referred to as the PAH 8 μm emission throughout this paper. While these stellar continuum-subtracted spectra may contain some thermal dust emission, most of the emission should originate from the PAH emission features, as has been demonstrated by Smith et al. (2007). We also calculated TIR surface brightnesses using

$$I(TIR) = 0.95\nu I_\nu(PAH8\ \mu m) + 1.15\nu I_\nu(24\ \mu m) + \nu I_\nu(70\ \mu m) + \nu I_\nu(160\ \mu m) \quad (9)$$

based on equation 22 from Draine & Li (2007).

In the analysis of these 45 arcsec regions, we assume that the background noise, which is measured in off-target regions in the images, is the only source of uncertainties that will affect this analysis. Uncertainties in the calibration will only scale the data, which does not affect either the slopes of lines fit to the data in log space or the scatter around the best fit lines. Uncertainties in the mean background value subtracted from the data should be negligible. The uncertainties for the ratios of surface brightnesses in two wave bands also includes a term to account for uncertainties in matching the coordinate systems of the two bands. This term is estimated from the standard deviations of the central four pixels in galaxies with symmetric, bright, point-like nuclei. In galaxies with such nuclei, the central four pixels should each sample approximately one-quarter of the peak of the central PSF. They should have the same surface brightness ratios if the image coordinate systems of different images are matched properly, but in practice, the ratios vary by small amounts. These terms, which are given in Table 2 for the ratios used in this paper, add uncertainties of approximately 5%-10%.

We also use maps of the (PAH 8 μm)/24 μm and (PAH 8 μm)/160 μm surface brightness ratios as additional aids in the interpretation of the data. To make these ratio maps, we again use the convolution kernels of K. D. Gordon to match the PSFs of the 3.6 and 8.0 μm images to the PSF in the longest wave band. Hence, the 3.6, 8.0, and 24 μm images used to produce the (PAH 8 μm)/24 μm maps have PSFs with FWHM of 6 arcsec, and the 3.6, 8.0, and 160 μm images used to produce the (PAH 8 μm)/160 μm maps have FWHM of 38 arcsec. The coordinate matching, IRAC background subtraction, IRAC aperture correction, and stellar continuum subtraction steps applied to the surface brightnesses measured in the 45 arcsec regions are also applied to the images used to make these ratio maps. Only pixels where the 24 μm data were detected at the 5σ level and where the PAH 8 and 160 μm data were detected at the 10σ level are shown in the maps. These thresholds were selected to filter out background noise and artefacts, which is why the threshold differs among the three wave bands. Moreover, pixels above these thresholds roughly correspond to the parts of the disc that were binned into the 45 arcsec regions described above. Additionally, foreground stars and any bright artefacts that remained in the data were masked out in the final ratio maps. Images of the PAH 8 μm emission, the (PAH 8 μm)/24 μm surface brightness ratio, and the (PAH 8 μm)/160 μm surface brightness ratio are shown in Figure 1.

3 COMPARISONS OF PAH 8 AND 24 μM EMISSION

The panels in the middle columns of Figure 1 show how the (PAH 8 μm)/24 μm surface brightness ratio varies within the discs of the galaxies. The resolution of the maps is 6 arcsec, which allows for seeing fine details within the images. If the PAH 8 μm surface brightness varies linearly with the 24 μm surface brightness, then this quantity should be constant across the discs of these galaxies. Instead, the (PAH 8 μm)/24 μm ratio is seen to vary significantly. In particular, the 24 μm emission peaks more strongly in point-like regions, which, according to the results from Calzetti et al. (2007) and Prescott et al. (2007), are HII regions. In contrast, the PAH 8 μm emission is stronger relative to the 24 μm emission in the diffuse interstellar regions. This is most apparent when comparing the arm and interarm regions of the grand-design spiral galaxies in this sample, notably NGC 628, NGC 3031, and NGC 5194. Some HII regions well outside the centres of the galaxies have very low (PAH 8 μm)/24 μm ratios even compared to the rest of the optical discs of the galaxies, as can be seen with the HII region in the northeast part of the disc in NGC 3184 and the HII region in the east part of the disc in NGC 3938.

Plots comparing colour to surface brightness are used here and in the next section to study the correlation between two wave bands. In a first-order approximation, the PAH 8, 24, and 160 μm surface brightnesses are all correlated with one another for these data. Hence, colour variations may be difficult to see or measure in plots directly comparing surface brightnesses in two wave bands. This is because the surface brightnesses vary by factors of $\sim$ 100 but the ratios of the surface brightnesses vary by less than a factor of 10. However, plots comparing surface brightness ratios to surface brightnesses can more clearly show deviations in the relation between two wave bands, including systematic variations in colour related to surface brightness. If a one-to-one correspondence exists between the PAH and 24 μm surface brightnesses, then the slopes of the best fit lines in these

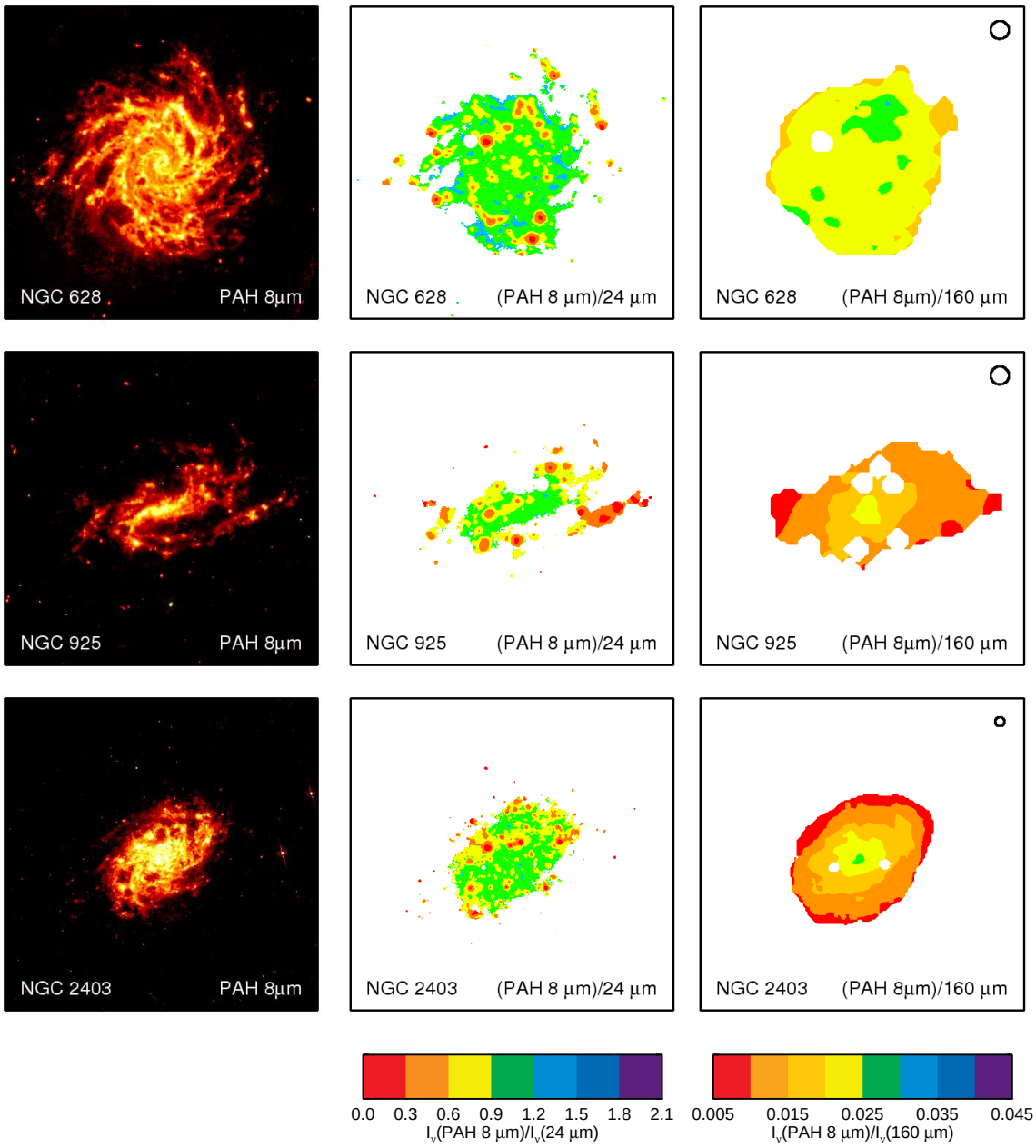

Figure 1. Images of the PAH 8 μm emission at the resolution of the IRAC data (left column), the (PAH 8 μm)/24 μm surface brightness ratio at the resolution of the 24 μm data (centre column), and the (PAH 8 μm)/160 μm surface brightness ratio at the resolution of the 160 μm data (right column) for the 15 galaxies studied in this analysis. The three maps for each galaxy are scaled to the same size. North is up and east is left in each map. The stellar continuum has been subtracted from the 8 and 24 μm bands to produce these maps. The contour levels in the ratio maps are chosen to show structure without showing excessive scatter from noise. The colour bars on this page give the values of the contour levels. The red colours in the ratio maps correspond to relatively weak PAH 8 μm emission, and the blue colours correspond to relatively strong PAH 8 μm emission. White regions in the ratio maps correspond to regions with low signal-to-noise ratios, regions with foreground stars, or regions strongly affected by artefacts in the data. In the PAH 8 μm image of NGC 3351, strips of data to the northeast and southwest of the centre have been strongly affected by muxbleed and have been masked out in the ratio maps. The circle in the top right corner of the (PAH 8 μm)/160 μm ratio maps shows the 38 arcsec FWHM of the 160 μm beam.

plots would be close to 0, and the scatter in these plots would be small. Such plots would be biased towards producing relations with slopes of -1 in log-log space if the two wave bands were randomly distributed. However, since the flux densities in all wave bands we studied here are approximately proportional to each other, such biases will not be present. To measure the physical (intrinsic) scatter around the best fit line, we will subtract the sum of the square of the measurement uncertainties from the sum of the square of the residuals from the best fit line. This is given by

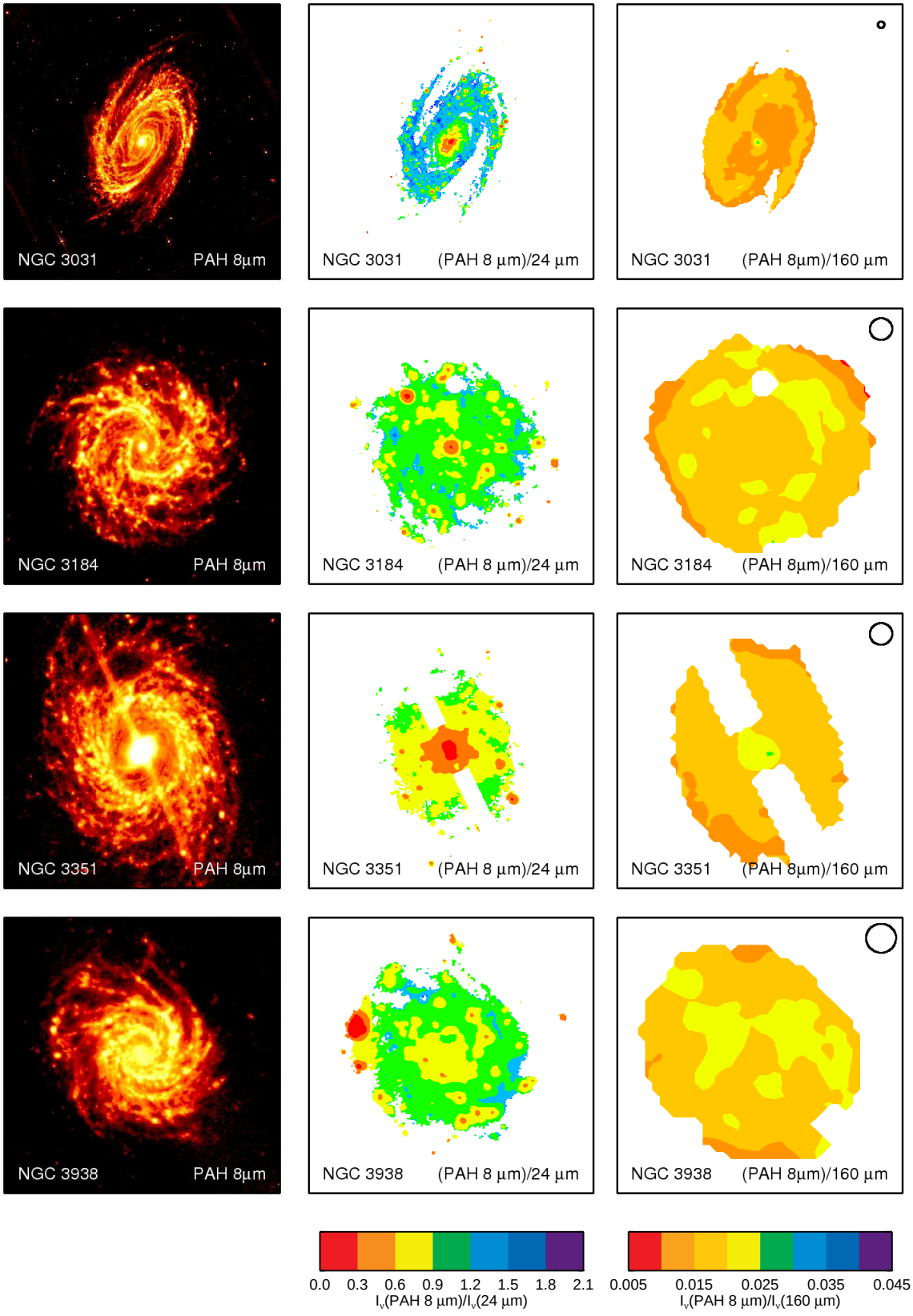

Figure 1 – continued

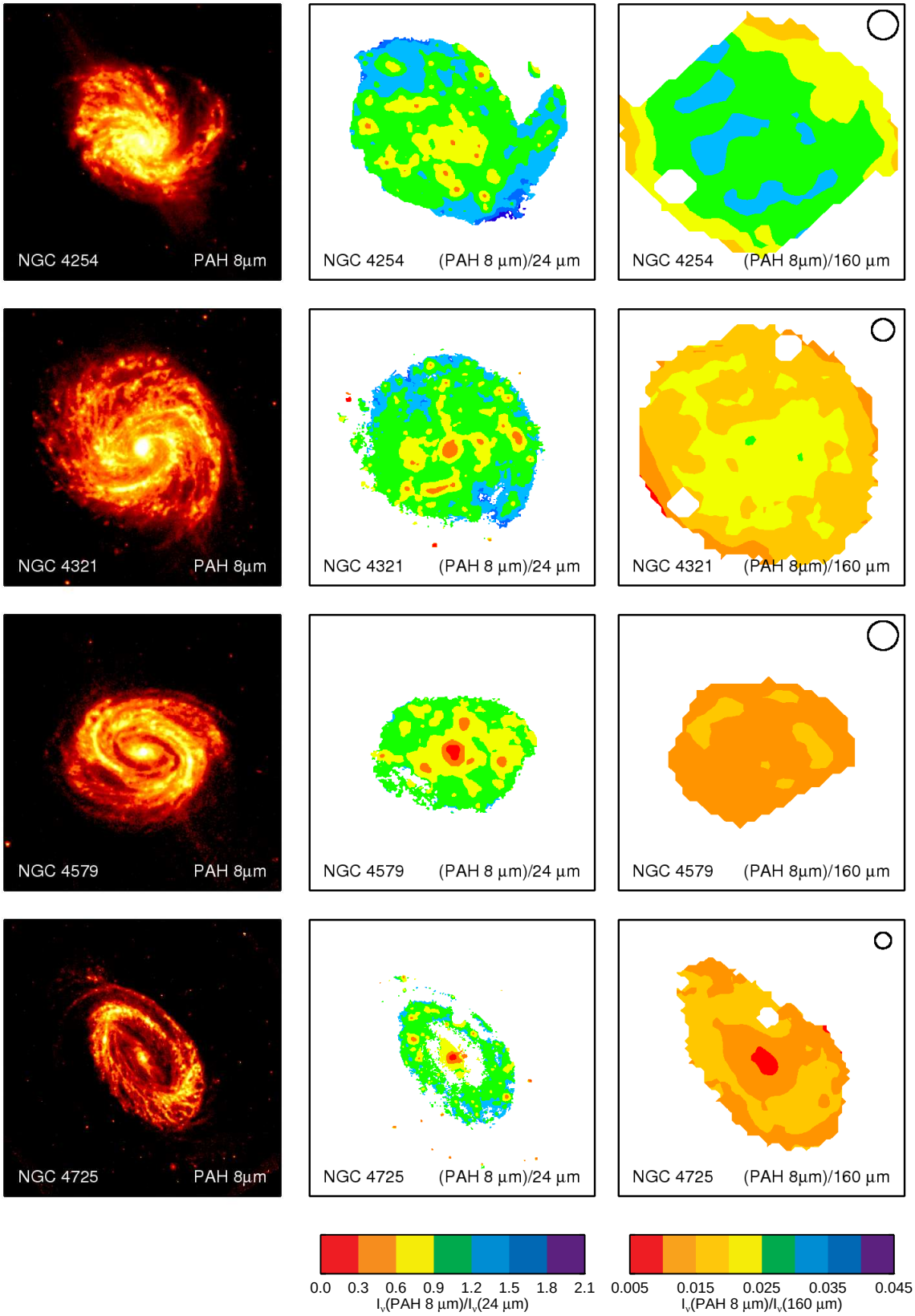

Figure 1 – continued

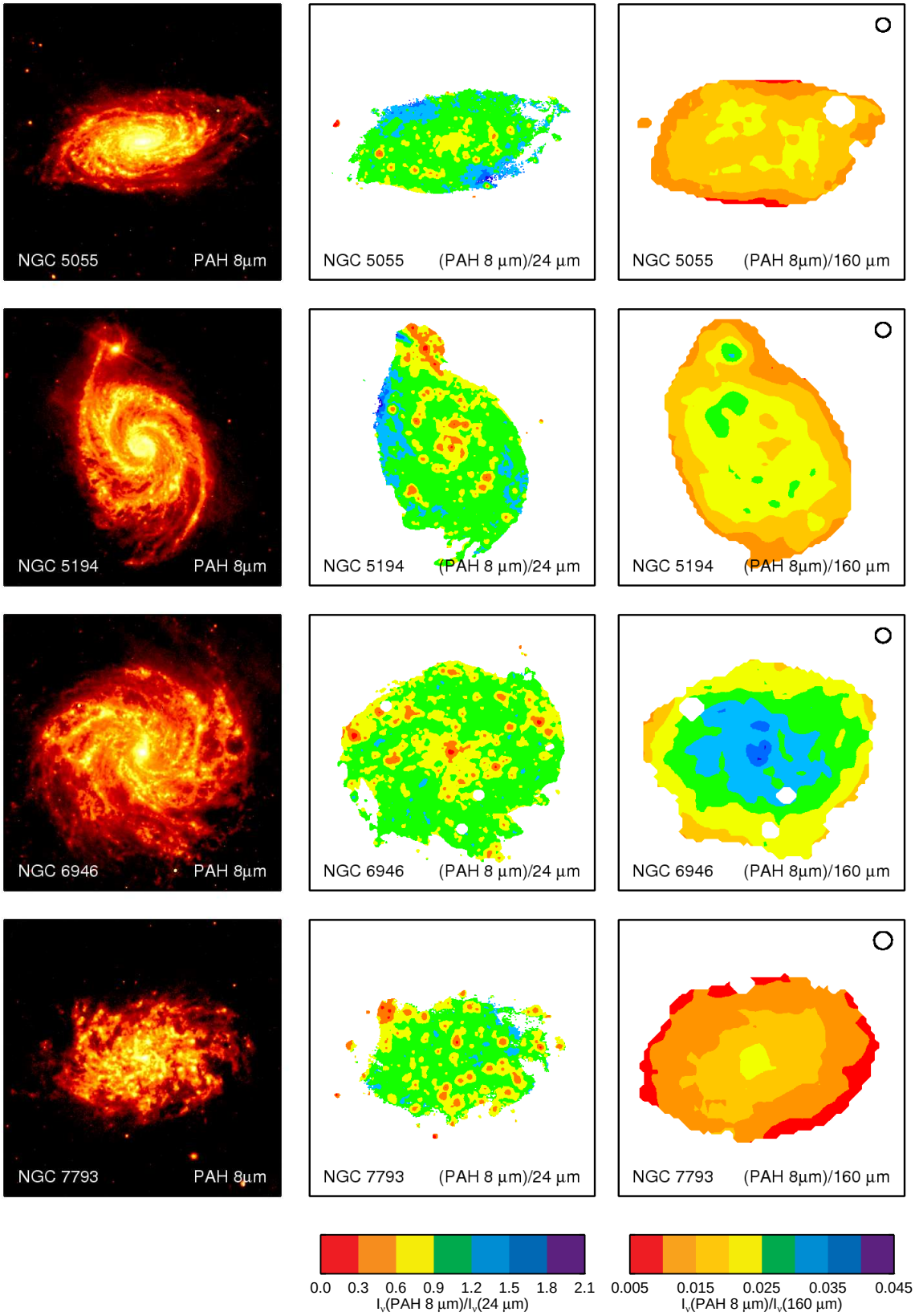

Figure 1 – continued

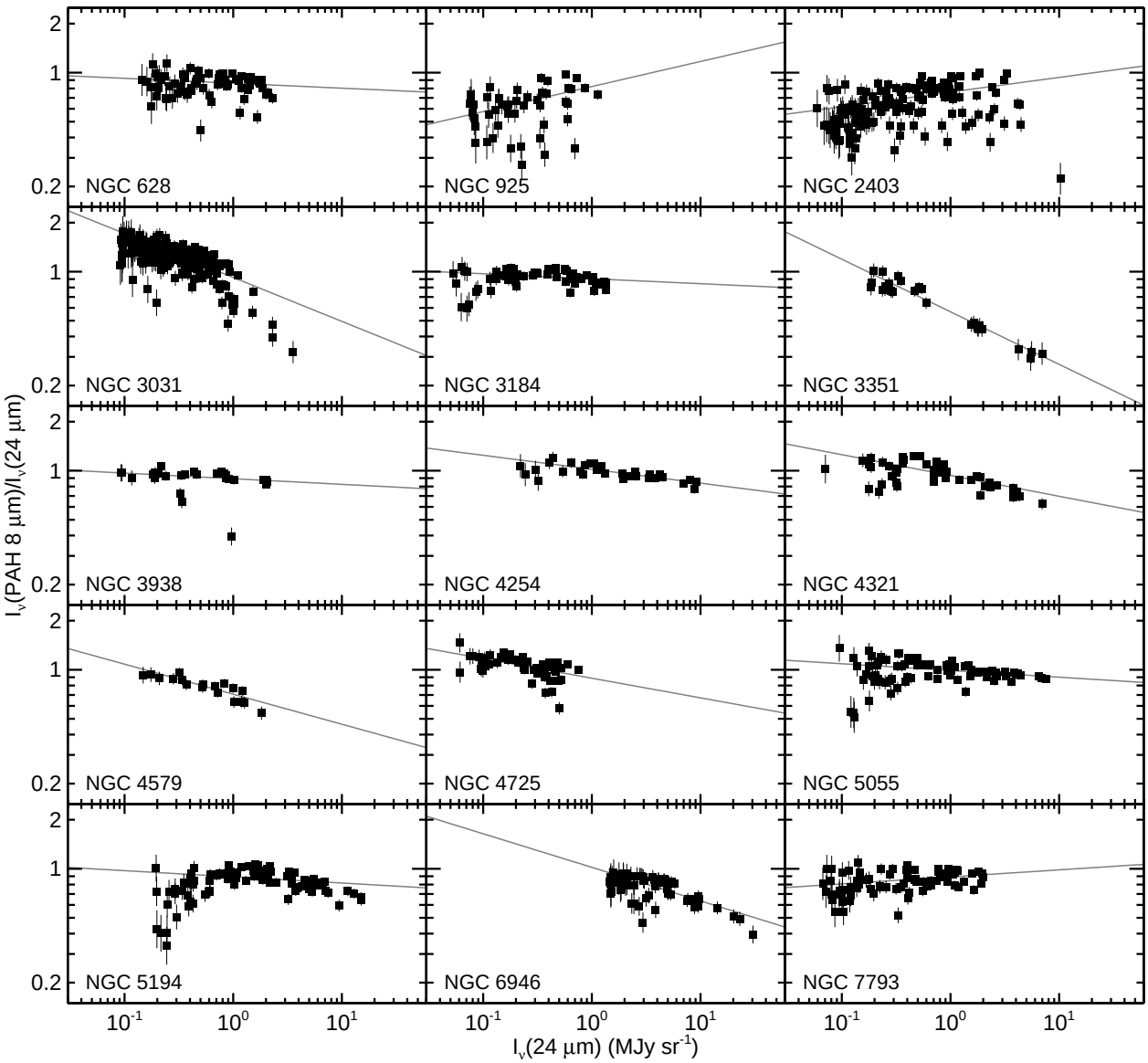

Figure 2. Plots of the (PAH 8 μm)/24 μm surface brightness ratios versus the 24 μm surface brightnesses for the 45 arcsec square regions measured in these galaxies. Note that the data are extracted from images with the same resolution as the 160 μm data. This was done so that resolution effects will not be a factor when comparing the data in this figure to the data in Figure 5. The grey lines are the best fitting lines for the relations in each plot; slopes and intrinsic scatters for these fits are given in Table 3. Note that the uncertainties in the x- and y-directions are used to weight the data in the fit.

$$s^2 = \sum (y_i - a - bx_i)^2 - \sum (\sigma_{xi}^2 + b^2\sigma_{yi}^2) \quad (10)$$

where x and y are abscissa and ordinate values with corresponding uncertainties σ_x and σ_y and a and b are the y-intercept and slope of of the best fit line. A value of 0 is reported if the result from Equation 10 is negative, as this would indicate that all of the scatter around the best fit line could be accounted for by the measurement uncertainties.

Figure 2 shows how the (PAH 8 μm)/24 μm ratio varies with 24 μm surface brightness among the 45 arcsec square regions described in Section 2.4. Note that the resolution of the data used in this figure is matched to the 38 arcsec resolution of the 160 μm images so that the results from these figures can be more easily compared to the results in Section 4. The slopes and intrinsic scatter for the best fit lines are given in Table 3. The best fitting lines are determined using uncertainties in both the x- and y-directions to weight the data, so the fits are strongly weighted towards high surface brightness regions.

The slopes of the best fit lines in Figure 2 are generally not statistically equivalent to 0, which demonstrates that the (PAH 8 μm)/24 μm ratio varies with surface brightness. In many galaxies (most notably NGC 3031, NGC 3351, and NGC 6946), the (PAH 8 μm)/24 μm ratio decreases notably as the 24 μm surface brightness increases. These tend to be galaxies with infrared-bright point-like nuclei. In a few

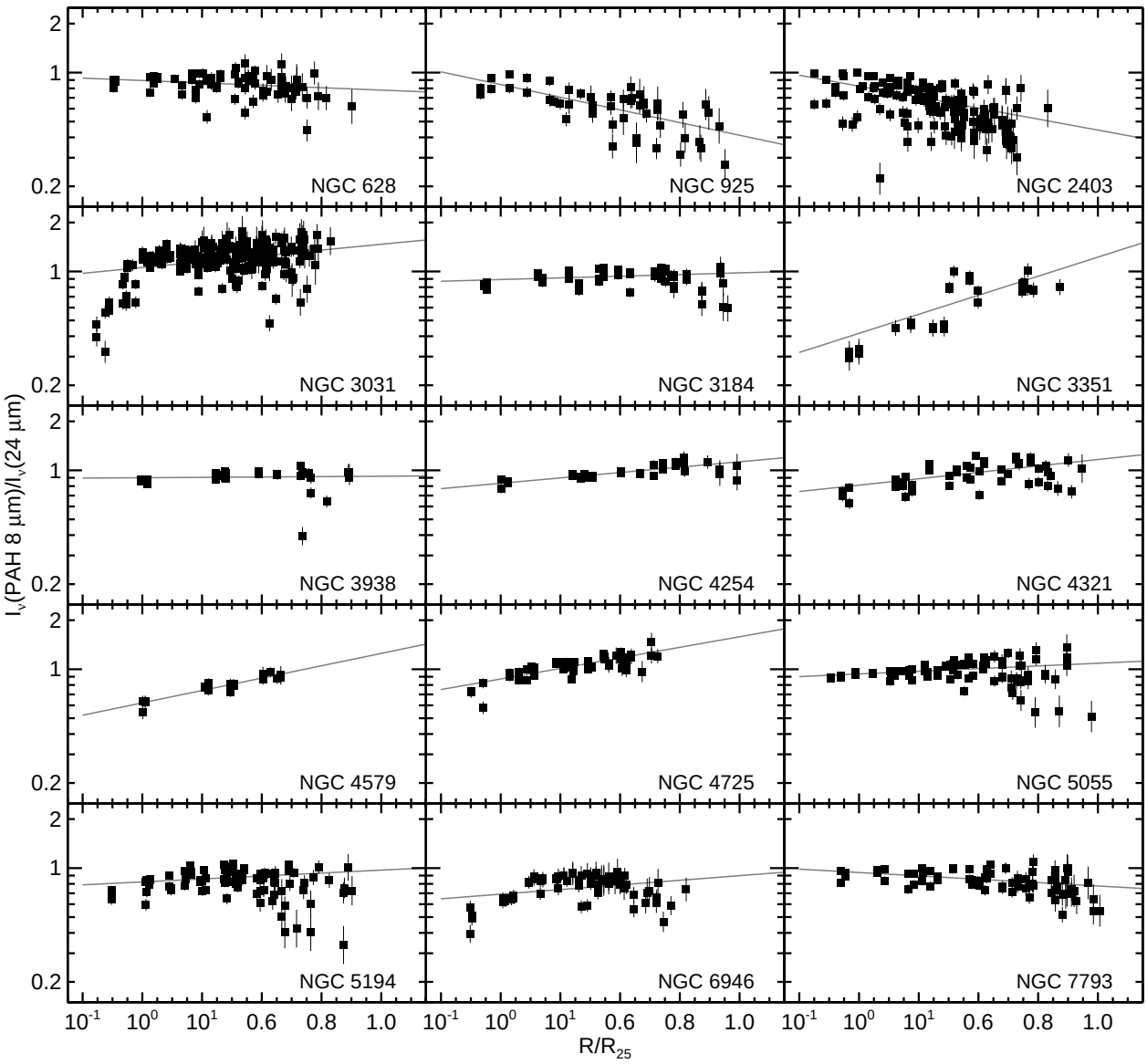

Figure 3. Plots of the (PAH 8 μm)/24 μm surface brightness ratios versus deprojected galactocentric radii for the 45 arcsec square regions measured in these galaxies. Note that the data are extracted from images with the same resolution as the 160 μm data. The radii are normalized by the radius of the D_{25} isophote given by de Vaucouleurs et al. (1991). The grey lines are the best fitting lines for the relations in each plot; slopes and intrinsic scatter for these fits are given in Table 6. Only the uncertainties in the (PAH 8 μm)/160 μm ratio are used to weight the data in the fit; the uncertainties in the radius are assumed to be negligible in this analysis.

other galaxies (NGC 2403 and NGC 7793, for example), the (PAH 8 μm)/24 μm ratio increases as the 24 μm surface brightness increases. The data for some galaxies also show a broad scatter, particularly for galaxies without infrared-bright nuclei. For a given 24 μm surface brightness, the (PAH 8 μm)/24 μm ratio varies by over a factor of 2 in high signal-to-noise regions in NGC 925 and NGC 2403. Although both of these galaxies are fit with linear relations in Figure 2, the broad scatter indicates that such a fit is unrealistic, so the (PAH 8) and 24 μm emission must be only weakly associated with each other. Also, some data points fall well below the best fit lines in Figure 2, particularly in the plots for NGC 2403 and NGC 3938. These regions correspond to very infrared-bright star-forming regions visible in Figure 1.

Figure 1 does not reveal the presence of any obvious dependence of the (PAH 8 μm)/24 μm on radius, but it is still useful to measure such gradients for comparison with abundance gradients, especially since it has been shown that the (PAH 8 μm)/24 μm ratio varies with metallicity (Engelbracht et al. 2005; Dale et al. 2005; Draine et al. 2007; Calzetti et al. 2007; Engelbracht et al. 2008). The relation between the (PAH 8 μm)/24 μm ratio and radius for the 45 arcsec square regions described in Section 2.4 is shown in Figure 3, with slopes for the best fit lines and intrinsic scatter given in Table 4. As in Figure 2, the slopes

Table 3. Slopes and Intrinsic Scatter for the Best Fit Line Describing (PAH 8) / 24 μm Surface Brightness Ratio versus 24 μm Surface Brightness Density[a]

Name	Slope	Intrinsic Scatter
NGC 628	-0.030 ± 0.015	0.20
NGC 925	0.15 ± 0.02	0.69
NGC 2403	0.090 ± 0.008	1.91
NGC 3031	-0.270 ± 0.011	0.93
NGC 3184	-0.030 ± 0.011	0.13
NGC 3351	-0.32 ± 0.02	0
NGC 3938	-0.035 ± 0.015	0.14
NGC 4254	-0.085 ± 0.013	0.0011
NGC 4321	-0.128 ± 0.010	0.14
NGC 4579	-0.18 ± 0.03	0
NGC 4725	-0.121 ± 0.017	0.12
NGC 5055	-0.041 ± 0.007	0.43
NGC 5194	-0.038 ± 0.008	0.89
NGC 6946	-0.21 ± 0.02	0.069
NGC 7793	0.043 ± 0.011	0.13

[a] These slopes and intrinsic scatter measurements are for the lines fit to the data in Figure 2. The data are measured within 45 arcsec bins in images with the same resolution as the 160 μm images. Intrinsic scatter measurements of 0 are reported when the value calculated with Equation 10 is negative; this indicates that measurement uncertainties can account for all of the scatter in the relation.

Table 4. Slopes and Intrinsic Scatter for the Best Fit Line Describing (PAH 8) / 24 μm Surface Brightness Ratio versus Radius[a]

Name	Slope	Intrinsic Scatter
NGC 628	-0.07 ± 0.02	0.16
NGC 925	-0.39 ± 0.03	0.23
NGC 2403	-0.34 ± 0.02	1.43
NGC 3031	0.178 ± 0.016	1.64
NGC 3184	0.051 ± 0.019	0.13
NGC 3351	0.59 ± 0.05	0.18
NGC 3938	0.01 ± 0.03	0.15
NGC 4254	0.17 ± 0.02	0
NGC 4321	0.20 ± 0.02	0.17
NGC 4579	0.38 ± 0.05	0
NGC 4725	0.32 ± 0.03	0.040
NGC 5055	0.082 ± 0.017	0.42
NGC 5194	0.09 ± 0.02	0.85
NGC 6946	0.14 ± 0.03	0.23
NGC 7793	-0.103 ± 0.018	0.091

[a] These slopes and intrinsic scatter measurements are for the lines fit to the data in Figure 3. The data are measured within 45 arcsec bins in images with the same resolution as the 160 μm images. Intrinsic scatter measurements of 0 are reported when the value calculated with Equation 10 is negative; this indicates that measurement uncertainties can account for all of the scatter in the relation.

vary significantly among the galaxies in this sample. Some galaxies with infrared-bright nuclei, such as NGC 3351 and NGC 4579, have large positive radial gradients in the (PAH 8 μm)/24 μm ratio, and in NGC 3031 and NGC 6946, the infrared-bright nuclei fall below the relation between the (PAH 8 μm)/24 μm ratio and radius. In a few other galaxies (most notably NGC 925 and NGC 2403), the radial gradient in the (PAH 8 μm)/24 μm ratio is negative. As in the relation between the (PAH 8 μm)/24 μm ratio versus 24 μm surface brightness, significant scatter is seen in some relations between the (PAH 8 μm)/24 μm ratio and radius, and some infrared-bright regions fall well below the best fit lines, as can be seen most clearly in NGC 2403 and NGC 3938. Further discussion concerning how these gradients might be related to radial gradients in abundances is presented in Section 5.1.

Overall, these data demonstrate that the relation between PAH 8 and 24 μm emission on spatial scales smaller than $\sim$ 2 kpc may exhibit a significant amount of scatter. Moreover, the relation between the (PAH 8 μm)/24 μm ratio and the 24 μm surface brightness does not vary in a way that is easily predictable within these galaxies.

4 COMPARISONS OF PAH 8 AND 160 μM EMISSION

The panels in the right columns of Figure 1 show how the (PAH 8 μm)/160 μm surface brightness ratio varies within the sample galaxies. The resolution of the maps is 38 arcsec. As with the (PAH 8 μm)/24 μm ratio, the (PAH 8 μm)/160 μm ratio does vary across the discs of these galaxies, although the variations are notably different. The (PAH 8 μm)/160 μm ratio generally appears to increase as the 160 μm surface brightness increases. Moreover, the (PAH 8 μm)/160 μm ratio also appears enhanced in large scale structures within the discs of these galaxies, such as the spiral arms in NGC 3031 and NGC 6946. In the centres of a few galaxies, the (PAH 8 μm)/160 μm ratio appears to decrease slightly. This is most apparent in NGC 3184, NGC 4725, and NGC 5055. The disc of NGC 4725 contains a ring, so the apparent decrease in the central (PAH 8 μm)/160 μm ratio could partly be related to an enhancement of the (PAH 8 μm)/160 μm ratio in the ring.

The maps also show that the (PAH 8 μm)/160 μm ratio does not necessarily peak in the extranuclear star-forming regions where local minima in the (PAH 8 μm)/24 μm ratio are found. This can be seen most dramatically in the images of NGC 2403, NGC 3184 and NGC 3938. To show that the differences between the (PAH 8 μm)/24 μm and (PAH 8 μm)/160 μm ratio maps is not a result of resolution effects for these three galaxies, we show both ratio maps for data at a resolution of 38 arcsec in Figure 4. Even at this resolution, the infrared-bright HII regions located in the northeast part of the disc near the nucleus of NGC 2403, in the northeast part of the disc in NGC 3184, and in the east part of the disc in NGC 3938 are still identifiable in the (PAH 8 μm)/24 μm ratio maps. However, these three infrared-bright HII regions are indistinguishable from the nearby dust emission in the (PAH 8 μm)/160 μm ratio maps. Nonetheless, keep in mind that enhancements in the (PAH 8 μm)/160 μm ratios are still visible in the large scale structures such as the spiral arms in NGC 3031 and NGC 6946.

Figure 5 shows how the (PAH 8 μm)/160 μm surface brightness ratio varies with 160 μm surface brightness among the sample galaxies, and the slopes and intrinsic scatter for the best fit lines as well as Spearman's correlation coefficients for the data are given in Table 5. Again, the best

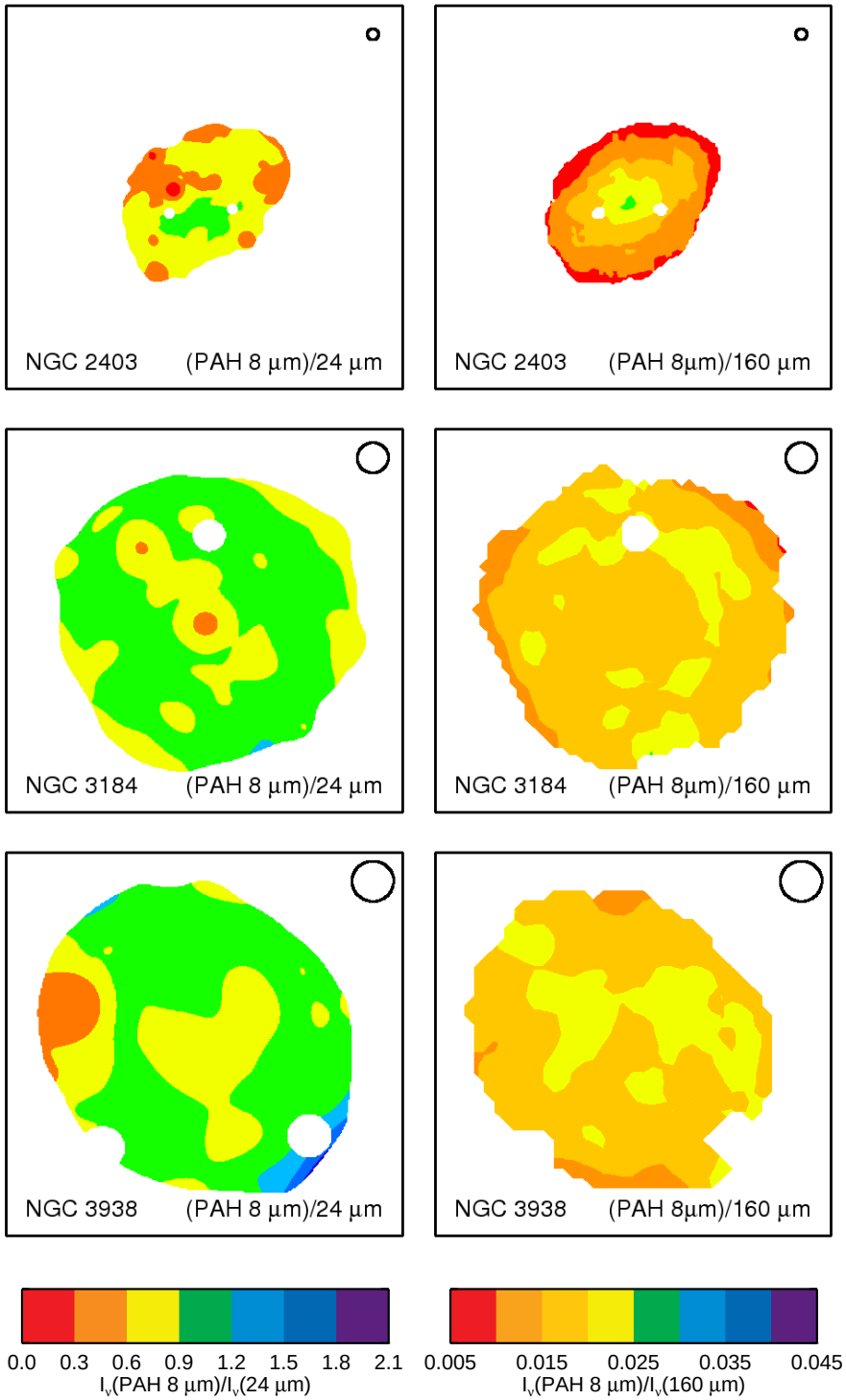

Figure 4. Images of the (PAH 8 μm)/24 μm surface brightness ratio at the resolution of the 160 μm data (left column), and the (PAH 8 μm)/160 μm surface brightness ratio at the resolution of the 160 μm data (right column) for three galaxies with extranuclear star-forming regions that are exceptionally bright at 24 μm. These maps demonstrate how the lower resolution affects the (PAH 8 μm)/24 μm ratio maps and how the maps still differ in comparison to the (PAH 8 μm)/160 μm ratio maps. The circle in the top right corner of each map shows the 38 arcsec FWHM of the 160 μm beam. See Figure 1 for additional information.

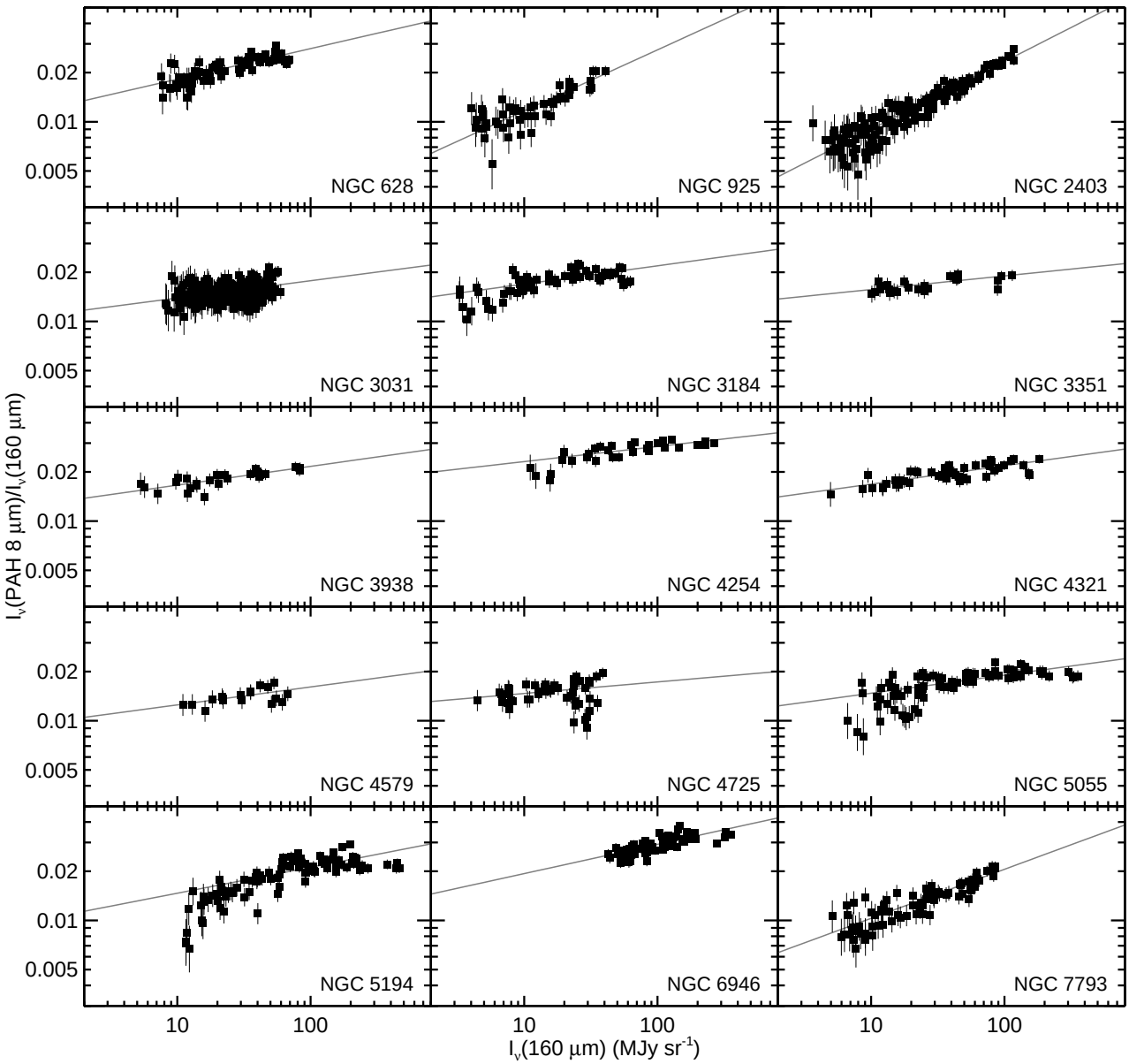

Figure 5. Plots of the (PAH 8 μm)/160 μm surface brightness ratios versus the 160 μm surface brightnesses for the 45 arcsec square regions measured in these galaxies. The grey lines are the best fitting lines for the relations in each plot; slopes, intrinsic scatter, and correlation coefficients for these fits are given in Table 5. Note that the uncertainties in the x- and y-directions are used to weight the data in the fit.

fitting lines are determined using uncertainties in both the x- and y-directions to weight the data.

For all galaxies in the sample, the (PAH 8 μm)/160 μm ratio generally increases as the 160 μm surface brightness increases, although the slopes of the relations are relatively shallow for some galaxies, such as NGC 3031, NGC 3351, and NGC 4725. If the slopes of the best fit lines in Figure 5 were equivalent to 0, this would indicate that a one-to-one correspondence exists between the PAH 8 and 160 μm bands. However, since the slopes are instead all positive, this indicates that the colours change from low to high surface brightness regions.

The scatter in the data around the best fit lines generally appears to be at the 10%-20% level in many cases. According to the intrinsic scatter measurement used here, the scatter in many of the plots can be explained mostly by uncertainties in the measurements. For most galaxies, the intrinsic scatter measurements in Table 5 are either similar to or notably lower than the values in Table 3. Because the data used for Tables 3 and 5 were measured in images that were degraded to the resolution of the 160 μm images, resolution effects should not be a factor in this comparison. Hence, this comparison between the intrinsic scatter measurements demonstrates quantitatively that the relation between PAH 8 and 160 μm emission may exhibit less scatter than the relation between PAH 8 and 24 μm emission.

Also note that very low and very high surface brightness 45 arcsec regions in NGC 5194 and NGC 5055 fall below the

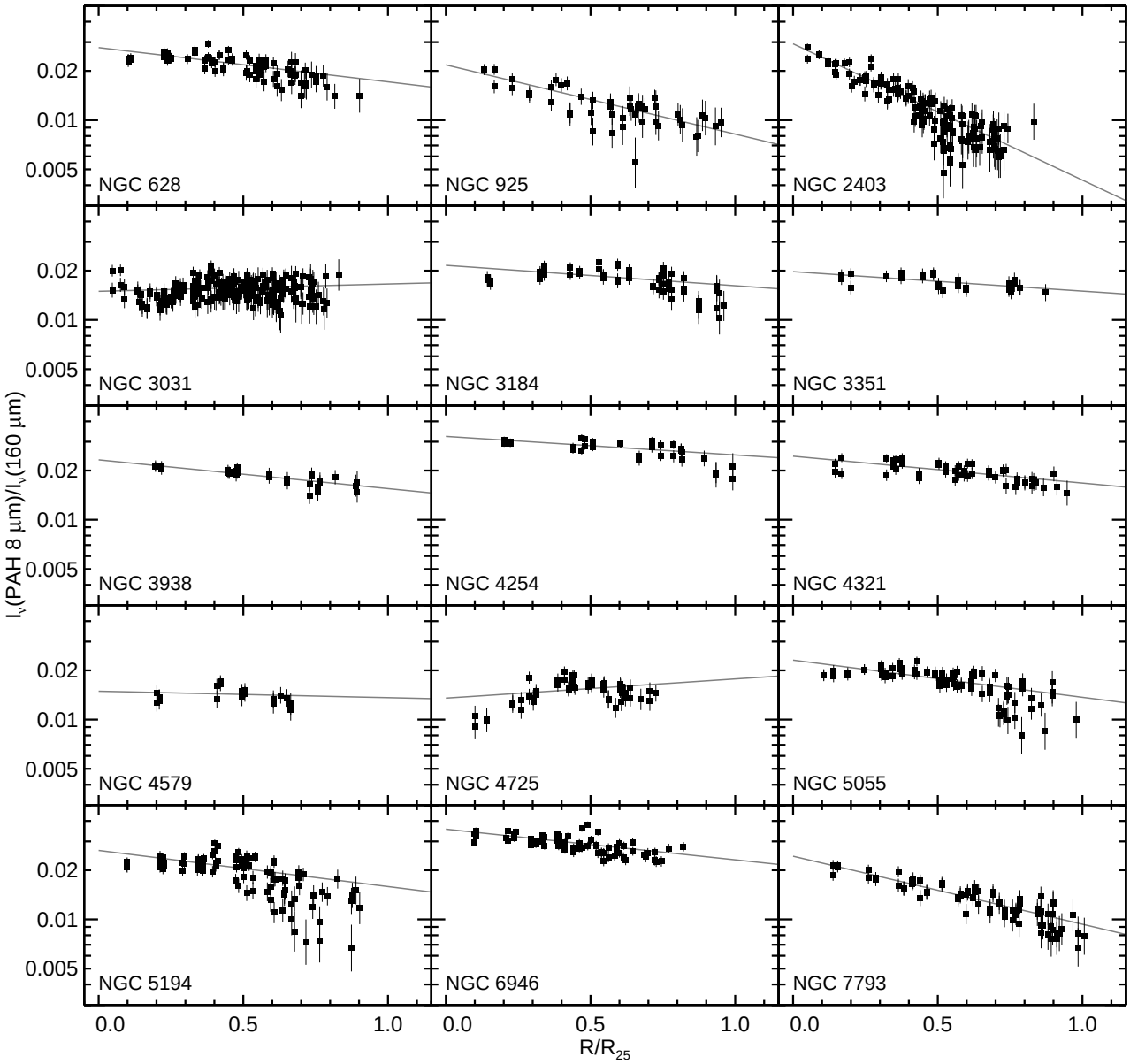

Figure 6. Plots of the (PAH 8 μm)/160 μm surface brightness ratios versus deprojected galactocentric radii for the 45 arcsec square regions measured in these galaxies. The radii are normalized by the radius of the D_{25} isophote given by de Vaucouleurs et al. (1991). The grey lines are the best fitting lines for the relations in each plot; slopes and intrinsic scatter for these fits are given in Table 6. Only the uncertainties in the (PAH 8 μm)/160 μm ratio are used to weight the data in the fit; the uncertainties in the radius are assumed to be negligible in this analysis.

best fit line. A related phenomenon is visible in NGC 4725, where the 45 arcsec regions within the inner ring fall below the best fit line in Figure 5. The disparity in the slopes between the high and low surface brightness data for some galaxies demonstrates that the (PAH 8 μm)/160 μm ratio either stops rising or decreases in the high surface brightness centres of the galaxies, as can also be seen in the maps of the (PAH 8 μm)/160 μm ratio in Figure 1 and in the plots of the (PAH 8 μm)/160 μm ratio versus radius in Figure 6.

Figure 1 illustrates how the (PAH 8 μm)/160 μm ratio may peak outside the nuclei of nearby galaxies. From the ratio maps alone, it is apparent that the (PAH 8 μm)/160 μm ratio does not necessarily monotonically decrease from the nuclei to the edges of the optical discs as was suggested by Bendo et al. (2006). Both Figure 6, which plots the (PAH 8 μm)/160 μm ratio versus deprojected galactocentric radius for 45 arcsec regions in these galaxies, and Table 6, which gives the slopes and intrinsic scatter measurements for the best fit lines in Figure 6 as well as the Spearman's correlation coefficient for the relations, support this conclusion. First, note that the regions with the highest (PAH 8 μm)/160 μm ratios within some of these galaxies are found outside the nucleus. As can be seen in Figure 1, the regions with enhanced (PAH 8 μm)/160 μm ratios may correspond to spiral structure, as is most clearly seen in NGC 3031 and NGC 6946. In NGC 4725, the inner ring has the highest

Table 5. Results for the Best Fit Line Describing (PAH 8) / 160 μm Surface Brightness Ratio versus 160 μm Surface Brightness[a]

Name	Slope	Intrinsic Scatter	Spearman's Rank Correlation Coefficient[b]
NGC 628	0.188 ± 0.018	0	0.85
NGC 925	0.37 ± 0.03	0	0.79
NGC 2403	0.415 ± 0.012	0	0.93
NGC 3031	0.11 ± 0.02	0	0.27
NGC 3184	0.112 ± 0.017	0.034	0.70
NGC 3351	0.08 ± 0.02	0	0.69
NGC 3938	0.12 ± 0.02	0	0.82
NGC 4254	0.093 ± 0.016	0.013	0.83
NGC 4321	0.113 ± 0.015	0	0.78
NGC 4579	0.11 ± 0.06	0	0.51
NGC 4725	0.07 ± 0.03	0.17	0.12
NGC 5055	0.111 ± 0.011	0.26	0.80
NGC 5194	0.159 ± 0.012	0.56	0.80
NGC 6946	0.179 ± 0.013	0.040	0.83
NGC 7793	0.300 ± 0.019	0	0.88

[a] These slopes and intrinsic scatter measurements are for the lines fit to the data in Figure 5. The data are measured within 45 arcsec bins in images with the same resolution as the 160 μm images. Intrinsic scatter measurements of 0 are reported when the value calculated with Equation 10 is negative; this indicates that measurement uncertainties can account for all of the scatter in the relation.
[b] The Spearman's rank correlation coefficient may have values between -1 and 1. A value close to 1 indicates a direct correlation between two values. A value close to -1 indicates an inverse correlation. A value of 0 indicates no correlation.

Table 6. Slopes and Intrinsic Scatter for the Best Fit Line Describing (PAH 8) / 160 μm Surface Brightness Ratio versus Radius[a]

Name	Slope	Intrinsic Scatter	Spearman's Rank Correlation Coefficient[b]
NGC 628	-0.21 ± 0.03	0.036	-0.80
NGC 925	-0.42 ± 0.04	0.038	-0.74
NGC 2403	-0.83 ± 0.03	0.29	-0.88
NGC 3031	0.05 ± 0.02	0	0.11
NGC 3184	-0.125 ± 0.03	0.11	-0.68
NGC 3351	-0.12 ± 0.04	0	-0.68
NGC 3938	-0.18 ± 0.04	0	-0.84
NGC 4254	-0.11 ± 0.02	0.039	-0.74
NGC 4321	-0.16 ± 0.02	0.00177	-0.73
NGC 4579	-0.04 ± 0.08	0	-0.32
NGC 4725	0.12 ± 0.05	0.130	0.18
NGC 5055	-0.23 ± 0.02	0.28	-0.79
NGC 5194	-0.22 ± 0.02	1.07	0.71
NGC 6946	-0.188 ± 0.016	0.069	-0.73
NGC 7793	-0.42 ± 0.03	0	-0.90

[a] These slopes and intrinsic scatter measurements are for the lines fit to the data in Figure 6. The data are measured within 45 arcsec bins in images with the same resolution as the 160 μm images. Intrinsic scatter measurements of 0 are reported when the value calculated with Equation 10 is negative; this indicates that measurement uncertainties can account for all of the scatter in the relation.
[b] The Spearman's rank correlation coefficient may have values between -1 and 1. A value close to 1 indicates a direct correlation between two values. A value close to -1 indicates an inverse correlation. A value of 0 indicates no correlation.

(PAH 8 μm)/160 μm ratio, not the nucleus. The intrinsic scatter in the fits versus surface brightness is generally lower than for those for the fits versus radius. Moreover, the Spearman's correlation coefficients for the relations between the (PAH 8 μm)/160 μm ratio and 160 μm surface brightness generally has a higher absolute value than the corresponding correlation coefficients for the relation between the (PAH 8 μm)/160 μm ratio and radius. These results suggest that the ratio may be more strongly dependent on 160 μm surface brightness than radius.

Since the (PAH 8 μm)/160 μm ratio may be dependent on dust heating, we also examine how the ratio is related to the 24 μm/160 μm ratio. The 24 μm band, which traces $\gtrsim$100 K hot dust emission, increases faster than other infrared band (including the PAH 8 and 160 μm bands) as the illuminating radiation field increases (Dale et al. 2001; Li & Draine 2001; Draine & Li 2007). The 160 μm band is approximately directly proportional to the TIR flux, as discussed in Section 2.1. Therefore, the 24 μm/160 μm ratio should be a reasonable indicator of dust heating. If the mass fraction of PAHs remains constant and if the (PAH 8 μm)/160 μm ratio is dependent on dust heating, then the (PAH 8 μm)/160 μm ratio should monotonically increase as the 24 μm/160 μm ratio increases, although the slope may not necessarily be constant. This comparison is similar to the direct comparison between the PAH 8 and 24 μm bands performed in Section 3, but the normalisation with the 160 μm band removes variations related to dust surface density.

Figure 7 shows how the (PAH 8 μm)/160 μm ratio varies with the 24 μm/160 μm ratio within 45 arcsec regions in the sample galaxies. Many of the 45 arcsec regions that are relatively weak in 24 μm emission tend to show a tight correspondence between the (PAH 8 μm)/160 μm and 24 μm/160 μm ratios, but some regions with enhanced 24 μm emission appear far to the right of these curves. The most spectacular example is NGC 3938, where the ratios for most of the regions closely follow a linear relation but the HII region on the east side of the disc falls far to the right of this relation. The relation between the two ratios on the left side of the panels in Figure 7 suggest that the (PAH 8 μm)/160 μm ratio is dependent on dust heating, but the outliers on the right in these panels show PAH 8 μm emission is not enhanced in areas with strong dust heating such as HII regions. Further interpretation of these results is presented in the next section.

For another perspective on the nature of the variation in the (PAH 8 μm)/160 μm ratio, we examined how the 160 μm/TIR and (PAH 8 μm)/TIR ratios vary as a function of TIR surface brightness. These are displayed in Figures 8 and 9, with slopes for the best fit lines given in Table 7 and Table 8. As stated in Section 2.1, the 160 μm/TIR ratio should gradually decrease as dust temperatures increase above $\sim$ 15 K. This is reflected in the general trends visible in Figure 8. Some scatter is visible in this figure, but this is expected, as the ratio will deviate from this general trend where 24 μm emission is strongly enhanced within star forming regions. The (PAH 8 μm)/TIR ratio is constant or

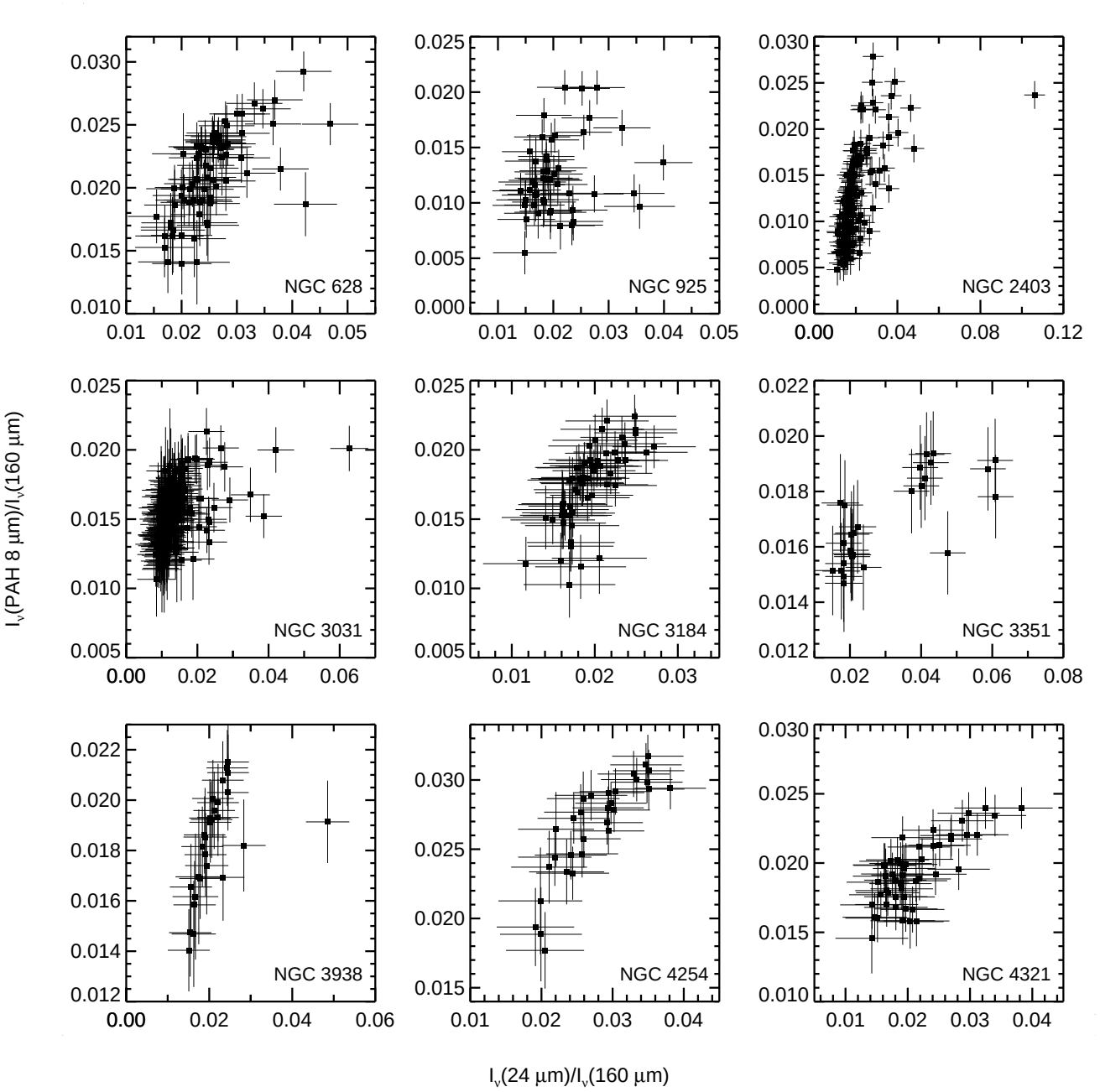

Figure 7. Plots of the (PAH 8 μm)/160 μm surface brightness ratios versus the 24 μm/160 μm surface brightness ratios for the 45 arcsec square regions measured in these galaxies. The 24 μm/160 μm ratios are used as a proxy for dust heating here.

changes very little in many galaxies (e.g. the slope of the best fit line in Figure 9 deviates less than 3σ from 0), which indicates that the (PAH 8μm) emission is directly proportional to TIR emission in these galaxies. Some scatter related to the scatter seen in Figure 2 is visible in these data, and in some cases, the infrared-brightest regions near the nucleus deviate from the trend in (PAH 8 μm)/TIR ratio versus TIR surface brightness, which makes the best fit lines appear positive. In a few exceptional galaxies, however, the (PAH 8 μm)/TIR ratio increases as TIR surface brightness increases. We conclude that the variations in (PAH 8 μm)/160 μm ratio are driven by changes in 160 μm emission relative to total dust emission in all galaxies and also by changes in (PAH 8 μm) emission relative to total dust emission in some situations. This is discussed further in the following section.

5 DISCUSSION

5.1 Interpretation of the relation between PAH 8 and 24 μm emission

The results in Section 3 as well as 4 demonstrate that the relation between PAH 8 and 24 μm emission exhibits a significant scatter on spatial scales smaller than $\sim$ 2 kpc. In

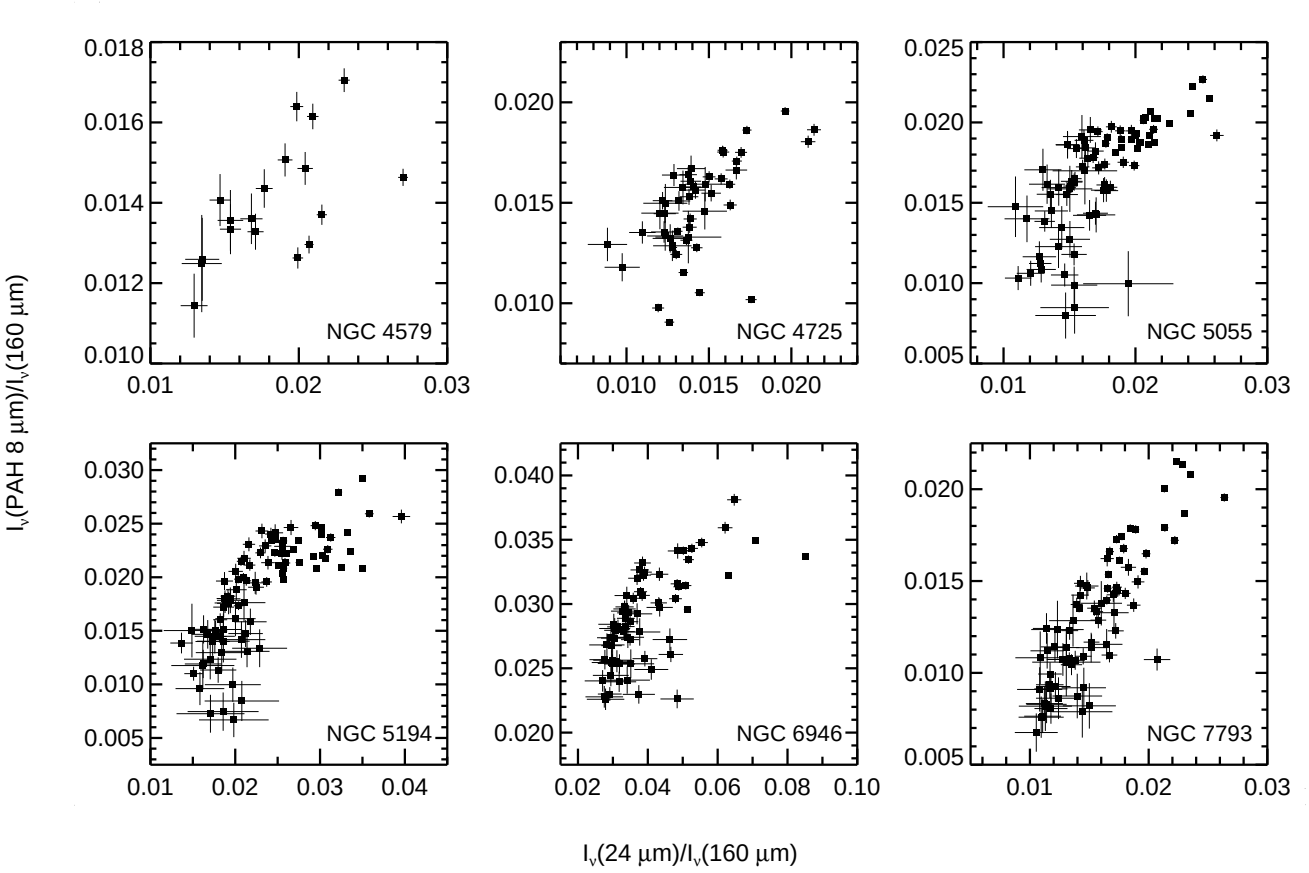

Figure 7 – continued

contrast, some ISO results from comparisons of 7 and 15 μm emission had implied that the ratio of PAH to hot dust emission should be relatively uniform across the discs of most galaxies (e.g. Roussel et al. 2001). However, some ISO studies actually found significant variations in the 7 μm/15 μm ratio (Haas et al. 2002), and even studies that did find uniform 7 μm/15 μm colours within the discs of galaxies noted that the ratio might decrease within starbursts in the centres of some galaxies (Roussel et al. 2001). The variations in the (PAH 8 μm)/24 μm ratio observed in this subsample of SINGS galaxies are consistent with Spitzer results for individual galaxies, such as for M51 (Calzetti et al. 2005), M81 (Perez-Gonzalez et al. 2006), and NGC 4631 (Bendo et al. 2006). Moreover, we find that 24 μm emission is more peaked in the centres of HII regions while the PAH 8 μm emission is relatively stronger outside HII regions, which is consistent with similar phenomena observed in NGC 300 (Helou et al. 2004), NGC 4631 (Bendo et al. 2006), and M101 (Gordon et al. 2008).

The variations in the (PAH 8 μm)/24 μm ratio are best seen by comparing bright star-forming regions and diffuse regions. If, because of the limited sensitivity of the data, the ratio between PAH and hot dust emission is only measured in the bright regions in some galaxies, as was done by Roussel et al. (2001), then the ratio between PAH and hot dust emission may appear uniform. When these bright regions are compared to diffuse emission, however, variations may be seen in the ratio of PAH to hot dust emission. This may be the primary reason why some results from ISO suggested that the ratio of PAH to hot dust emission was uniform in most spiral galaxies whereas variations may be seen in Spitzer data.

Additionally, differences between the nature of 15 and 24 μm dust emission could have also contributed to the differences between the 7 μm/15 μm relation observed with ISO and the (PAH 8 μm)/24 μm relation observed with Spitzer. Based on semi-empirical and theoretical models, the 24 μm band is expected to increase faster than the 15 μm as the illuminating radiation field increases (Dale et al. 2001; Li & Draine 2001; Draine & Li 2007). Moreover, unlike the 24 μm band, a significant fraction of the 15 μm band includes PAH emission (Smith et al. 2007; Draine & Li 2007). Consequently, a comparison of PAH to 24 μm data should exhibit more scatter than a comparison of PAH to 15 μm data.

We also found that differences in the distribution of star-forming regions within galaxies could influence how the (PAH 8 μm)/24 μm ratio varies with 24 μm surface brightness. In some galaxies, such as NGC 3351 and NGC 6946, the nucleus is the strongest site of star formation. Hence, the location expected to have the lowest (PAH 8 μm)/24 μm ratio will correspond to the location with the highest 24 μm surface brightness, so the data will show that the (PAH 8 μm)/24 μm ratio decreases as the 24 μm surface brightness increases, thus varying as expected from many models of dust emission (e.g. Dale et al. 2001; Li & Draine 2001;

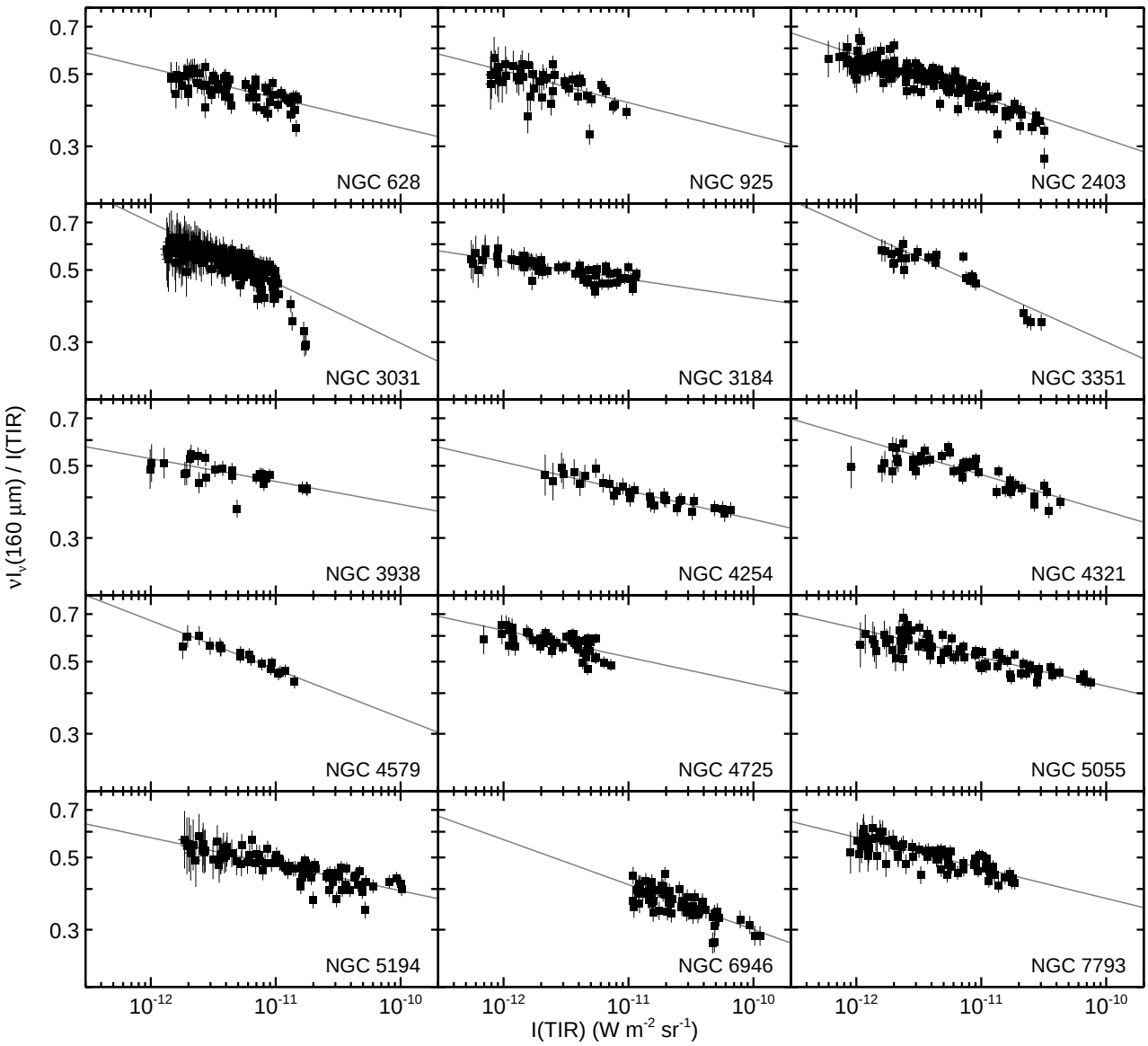

Figure 8. Plots of the 160 μm/TIR surface brightness ratios versus TIR surface brightness for the 45 arcsec square regions measured in these galaxies. The grey lines are the best fitting lines for the relations in each plot; slopes for these fits are given in Table 7. Note that the uncertainties in the x- and y-directions are used to weight the data in the fit.

Draine & Li 2007). In other galaxies, such as NGC 925 and NGC 2403, the nucleus is not the site of the strongest star formation activity, and many HII regions can be found at the periphery of the regions that were detected at the 3σ level in these data. While point-like 24 μm sources should correspond to HII regions (Prescott et al. 2007; Calzetti et al. 2007), dust emission models such as those presented by Li & Draine (2001), Dale et al. (2001), and Draine & Li (2007) suggest that diffuse 24 μm dust emission may still potentially originate from regions outside star-forming regions with high radiation fields. Furthermore, ionising photons may escape from star-forming regions into the diffuse interstellar medium (Oey et al. 2007), and results from Calzetti et al. (2007) suggest that 24 μm emission may trace the recombination line emission from the diffuse gas heated by these photons. Hence, it is possible that the infrared-brightest regions in the centres of some galaxies may contain a higher fraction of 24 μm emission from diffuse dust than the infrared-faint regions, so the (PAH 8 μm)/24 μm ratio will increase as the 24 μm surface brightness increases, as can be seen for NGC 925 and NGC 2403 in Figure 2.

Several mechanisms may be responsible for creating the differences in the spatial distribution of the PAH 8 and 24 μm emission. First, as the illuminating radiation field increases, the 24 μm band is thought to increase more rapidly than bands that trace PAH emission (Dale et al. 2001; Li & Draine 2001; Draine & Li 2007). Therefore, the 24 μm emission may be more strongly enhanced than the PAH emission in regions with very high radiation fields, such as star-forming regions. Second, the PAHs may be destroyed

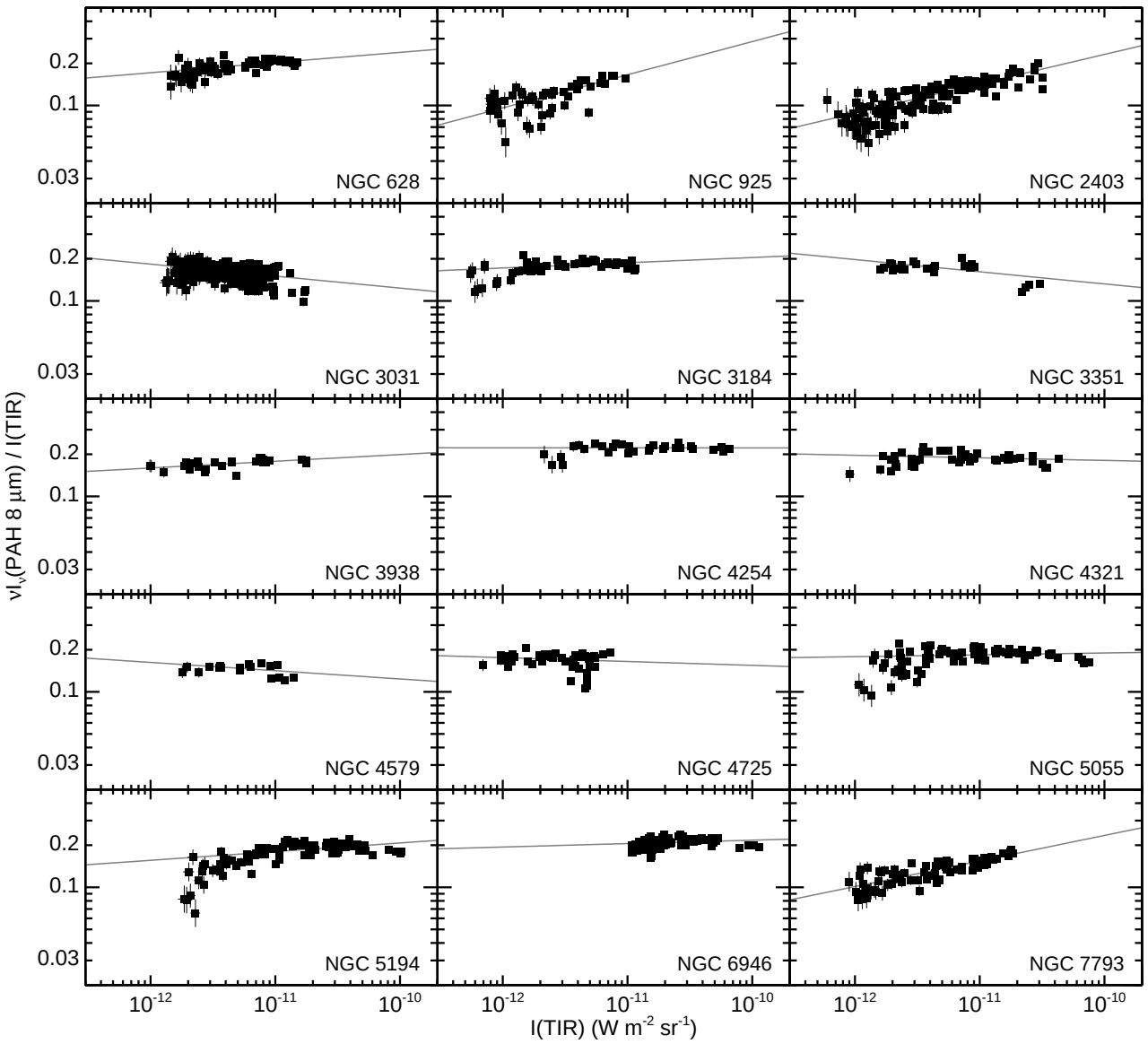

Figure 9. Plots of the (PAH 8 μm)/TIR surface brightness ratios versus TIR surface brightness for the 45 arcsec square regions measured in these galaxies. The grey lines are the best fitting lines for the relations in each plot; slopes for these fits are given in Table 8. Note that the uncertainties in the x- and y-directions are used to weight the data in the fit.

in regions with strong radiation fields or in regions with large numbers of high-energy photons (e.g. Madden et al. 2006). The PAHs would be absent, and the (PAH 8 μm)/24 μm ratio would be low in the centres of star-forming regions and AGN. Third, the ratio of the 7.7 μm PAH feature to other PAH features may vary with changes in the charge state of the PAHs (e.g. Allamandola et al. 1999; Li & Draine 2001; Draine & Li 2007). This could occur in HII regions if the electron densities are high enough that recombination rates becomes significant compared to photoionisation rates, which would lead to a reduction of the PAH^+ ions that produce the 7.7 μm emission (Weingartner & Draine 2001).

While the enhancement of 24 μm emission linked to dust heating in star-forming regions is certainly at least part of the reason why the (PAH 8 μm)/24 μm ratio varies, we argue that the variations must also be caused in part by a reduction in PAH emission in the 8 μm band through either PAH destruction or changes in the relative strengths of PAH spectral features. Models of dust emission have suggested that, if PAHs are present and radiating at 8 μm, the (PAH 8 μm)/160 μm ratio would be enhanced in regions with very strong radiation fields, warmer dust, and low (PAH 8 μm)/24 μm ratios (Draine & Li 2007). However, the (PAH 8 μm)/160 μm ratio does not peak within individual star-forming regions where local minima in the (PAH 8 μm)/24 μm ratio are found, such as the bright extranuclear regions in NGC 2403, NGC 3184, and NGC 3938. This is best demonstrated by comparisons of the maps of (PAH 8 μm)/24 μm and (PAH 8 μm)/160 μm ratios at matching resolutions in Figure 4, although the additional discussion

Table 7. Results for the Best Fit Line Describing 160 μm / TIR Surface Brightness Ratio versus TIR Surface Brightness

Name	Slope[a]
NGC 628	-0.092 ± 0.011
NGC 925	-0.098 ± 0.017
NGC 2403	-0.130 ± 0.005
NGC 3031	-0.186 ± 0.012
NGC 3184	-0.057 ± 0.009
NGC 3351	-0.173 ± 0.013
NGC 3938	-0.070 ± 0.015
NGC 4254	-0.088 ± 0.014
NGC 4321	-0.113 ± 0.009
NGC 4579	-0.15 ± 0.02
NGC 4725	-0.083 ± 0.013
NGC 5055	-0.089 ± 0.006
NGC 5194	-0.082 ± 0.008
NGC 6946	-0.138 ± 0.013
NGC 7793	-0.094 ± 0.009

[a] These slopes are for the lines fit to the data in Figure 8. The data are measured within 45 arcsec bins in images with the same resolution as the 160 μm images.

Table 8. Results for the Best Fit Line Describing (PAH 8 μm) / TIR Surface Brightness Ratio versus TIR Surface Brightness

Name	Slope[a]
NGC 628	0.073 ± 0.012
NGC 925	0.237 ± 0.018
NGC 2403	0.210 ± 0.006
NGC 3031	-0.086 ± 0.011
NGC 3184	0.037 ± 0.009
NGC 3351	-0.087 ± 0.012
NGC 3938	0.048 ± 0.012
NGC 4254	0.000 ± 0.010
NGC 4321	-0.018 ± 0.007
NGC 4579	-0.06 ± 0.03
NGC 4725	-0.028 ± 0.013
NGC 5055	0.013 ± 0.006
NGC 5194	0.062 ± 0.006
NGC 6946	0.024 ± 0.008
NGC 7793	0.183 ± 0.010

[a] These slopes are for the lines fit to the data in Figure 9. The data are measured within 45 arcsec bins in images with the same resolution as the 160 μm images.

in Section 4 and the maps in Figure 1 also support this conclusion. Furthermore, Figure 7 demonstrates that the (PAH 8 μm)/160 μm ratios are not always higher in regions with strongly enhanced 24 μm emission. According to the models of Draine & Li (2007), the (PAH 8 μm)/160 μm should monotonically increase with the 24 μm/160 μm ratio in these regions if PAHs are present and if the PAH ionisation does not change. These results indicate that the variations in the (PAH 8 μm)/24 μm ratio must be in part caused by the suppression of PAH 8 μm emission.

Observations of individual HII regions within the Milky Way have shown that the PAH emission may be found primarily in shell-like structures around the star-forming regions (e.g. Rho et al. 2006; Churchwell et al. 2006; Smith & Brooks 2007) and that the strength of all PAH spectral features relative to 24 μm hot dust emission decreases within the centres of HII regions (e.g. Povich et al. 2007; Lebouteiller et al. 2007). If these results are applicable to the galaxies in this paper, then the inferred decrease in the (PAH 8 μm)/24 μm ratio within star-forming regions may also be partly caused by PAH destruction and not just variations in the strengths of PAH spectral features. Further work with mid-infrared spectroscopic observations of star-forming regions within these galaxies, specifically studies of how the total emission in all PAH spectral feature emission varies with respect to total dust emission, would be needed to confirm that PAH destruction is taking place.

Although the PAH 8 μm emission does not share a one-to-one correspondence with 24 μm emission or with other star formation tracers on kiloparsec scales, this does not necessarily preclude its use as a tracer of integrated star formation within nearby spiral galaxies. The variations between PAH 8 μm emission and other star formation tracers could potentially be averaged out when integrating across the optical discs of spiral galaxies. However, because a significant fraction of the PAH 8 μm emission still originates from the diffuse ISM, it would not be as reliable as other global star formation tracers. Furthermore, because the ratio of PAH to TIR flux and the ratio of PAH to 24 μm flux density varies with metallicity (Engelbracht et al. 2005; Dale et al. 2005; Draine et al. 2007; Calzetti et al. 2007; Engelbracht et al. 2008), a conversion factor relating integrated PAH 8 μm emission to star formation may also vary with global metallicity.

We also note that variations in metallicity could possibly produce variations in the (PAH 8 μm)/24 μm ratio observed in the galaxies studied in this paper, but these variations would not be expected to cause the differences in the ratio between star-forming regions and the diffuse ISM observed here. Moreover, the gas-phase abundances of the galaxies in our sample are well above 12+log(O/H)$\simeq$8-8.1, where PAH 8 μm emission should be suppressed as determined by Draine et al. (2007) and Engelbracht et al. (2008), although NGC 628, NGC 925, NGC 2403, and NGC 3031 all have characteristic abundances close to this value and might be affected. To examine this issue further, we compared the radial gradients in the (PAH 8 μm)/24 μm ratio to the radial gradients in 12+log(O/H) measured by J. Moustakas et al. (2008, in preparation) using the Pilyugin & Thuan (2005) calibration for 13 of the galaxies in our sample. (Abundance gradients are not given by J. Moustakas et al. for NGC 3938 and NGC 4579, and so these galaxies are not included in this comparison.) The relation between these two radial gradients can be seen in Figure 10. If the variations in the (PAH 8 μm)/24 μm ratio depended primarily on metallicity variations, then we would expect to see a correlation between the gradients in Figure 10. However, the two gradients appear uncorrelated, which indicates that the variations in the (PAH 8 μm)/24 μm ratio that have been observed here depend primarily on effects unrelated to metallicity. This conclusion for these spiral galaxies is also consistent with the results presented for the spiral galaxy M101 by Gordon et al. (2008), who found that PAH equivalent widths appeared more dependent on the ionisation of the ISM (characterised using [NeIII]/[NeII] and [SIV]/[SIII]) than 12+log(O/H).

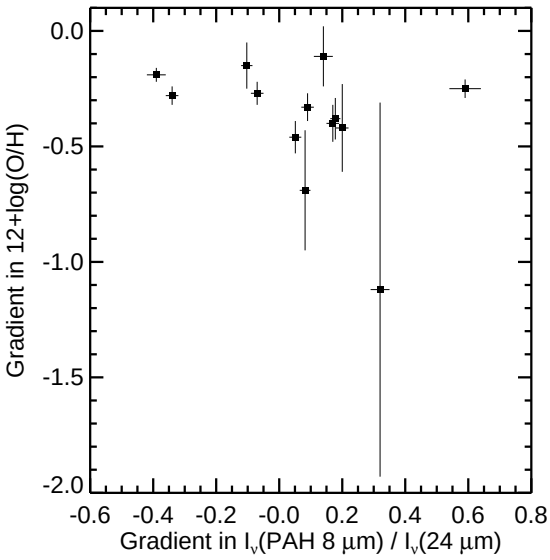

Figure 10. Plot of the radial gradients in the (PAH 8 μm)/24 μm ratio from Table 4 versus radial gradients in 12+log(O/H) measured by J. Moustakas et al. (2008, in preparation) using the Pilyugin & Thuan (2005) calibration. The gradients are in units of dex divided by the radius of the D_{25} isophote. Gradients in 12+log(O/H) were not provided for NGC 3938 and NGC 4579.

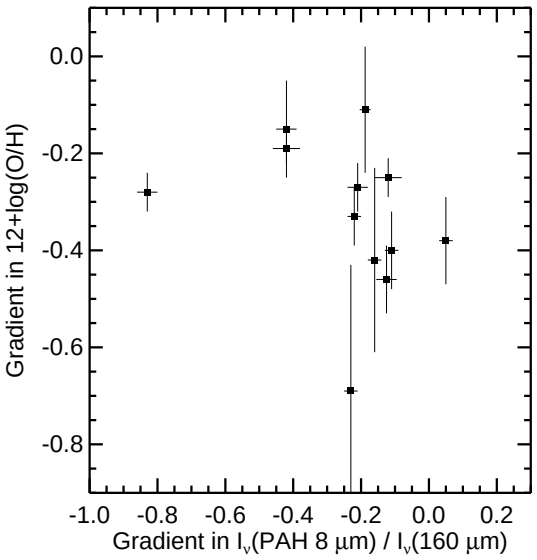

Figure 11. Plot of the radial gradients in the (PAH 8 μm)/160 μm ratio from Table 6 versus radial gradients in 12+log(O/H) measured by J. Moustakas et al. (2008, in preparation) using the Pilyugin & Thuan (2005) calibration. The gradients are in units of dex divided by the radius of the D_{25} isophote. Gradients in 12+log(O/H) were not provided for NGC 3938 and NGC 4579, and the gradients in the (PAH 8 μm)/160 μm ratio for NGC 4725 changes significantly between the centre and outer disc, so these three galaxies are not included in this plot.

5.2 Interpretation of the relation between PAH 8 and 160 μm emission

The (PAH 8 μm)/160 μm ratio appears to be closely correlated with the 160 μm surface brightness measured on 45 arcsec scales in most galaxies, even in nearby galaxies where this angular scale corresponds to $\lesssim$1 kpc. Moreover, the (PAH 8 μm)/160 μm ratio sometimes traces high surface brightness large scale structures in the discs of these galaxies, such as the spiral arms in NGC 3031 or NGC 6946. This indicates that the variations in the ratio may not be primarily dependent on radius as inferred by Bendo et al. (2006) but instead may be primarily dependent on the 160 μm surface brightness. However, the large scale structures within these galaxies are only marginally resolved in the 160 μm data. Higher resolution observations at wavelengths longer than 100 μm are needed to confirm that this interpretation is valid.

Nonetheless, if the above interpretation is correct, then it also suggests that the variations in the (PAH 8 μm)/160 μm ratio may be more dependent on 160 μm surface brightness than metallicity within the regions studied in these galaxies. Since variations in metallicity have been linked to decreased PAH emission relative to longer-wavelength dust emission in the integrated spectra of galaxies (e.g. Engelbracht et al. 2005; Dale et al. 2005; Draine et al. 2007; Engelbracht et al. 2008), it was not unreasonable to expect that the observed variations in the (PAH 8 μm)/160 μm ratio within these galaxies might be linked to metallicity variations. However, the 12+log(O/H) values measured in these galaxies by J. Moustakas et al. (2008, in preparation) generally do not drop below $\sim$ 8-8.1, which is where Draine et al. (2007) and Engelbracht et al. (2008) showed that metallicity strongly affects PAH 8 μm emission. Moreover, metallicity is expected to decrease monotonically with radius, while the (PAH 8 μm)/160 μm ratio and the 160 μm surface brightness do not, and the metallicity should not peak within substructures such as spiral arms, whereas the (PAH 8 μm)/160 μm ratio and the 160 μm surface brightness both peak within such substructures. As an additional test, we compared the gradients in the (PAH 8 μm)/160 μm ratio versus radius with the metallicity gradients from J. Moustakas et al. (2008, in preparation) calculated with the Pilyugin & Thuan (2005) calibration. For this comparison, we excluded NGC 4725 because the gradients in the (PAH 8 μm)/160 μm ratio changes significantly between the nucleus and the outer disc, and we excluded NGC 3938 and NGC 4579 because abundance gradients are not given by J. Moustakas et al. The gradients for the other galaxies are plotted in Figure 11. If the (PAH 8 μm)/160 μm ratio was affected by metallicity in the regions studied in these galaxies, then these data would be positively correlated. Since the data in Figure 11 do not exhibit such a correlation, the two gradients may be unrelated. We therefore conclude that, in the regions of the galaxies studied here, metallicity variations are not as important as 160 μm surface brightness variations in determining the (PAH 8 μm)/160 μm ratio, although metallicity may be a factor outside the optical discs. Again, this is consistent with the conclusions reached by Gordon et al. (2008), who found that PAH equivalent widths in M101 were more dependent on the ionisation of the ISM than abundances.

While the (PAH 8 μm)/160 μm ratio traces large scale structure, we have demonstrated that the ratio is not enhanced within individual star-forming regions, and we ex-

plained earlier in this section that PAH 8 μm emission must be inhibited in regions with strong radiation fields. Based on these conclusions and the strong relation between the (PAH 8 μm)/160 μm ratio and 160 μm surface brightness, we infer that the PAHs in these galaxies are generally associated with the cold ($\sim$ 20 K) dust that dominates the 160 μm emission, at least on scales of $\sim$ 2 kpc. Because most of this cold dust may be expected to be found in the diffuse ISM, the PAHs may also be found primarily in the diffuse ISM as well, although some of the cold dust and PAHs may also be found within clouds associated with star-forming regions. Moreover, since the (PAH 8 μm)/160 μm ratio increases as the 160 μm surface brightness increases, the (PAH 8 μm)/160 μm ratio may be an indicator of variations in the intensity of the radiation field heating the diffuse ISM. This is further supported by the tight correlation between the (PAH 8 μm)/160 μm ratio and the 24 μm/160 μm ratio found for many regions with weak 24 μm emission in Figure 7, which are presumably regions that primarily sample dust emission from the diffuse ISM. Nonetheless, this interpretation is only valid if the PAH mass fraction does not vary appreciably between infrared-faint and infrared-bright regions in the diffuse ISM, and far-infrared observations with higher angular resolution will be needed to determine whether this association is still applicable on smaller spatial scales.

In most galaxies in this sample, the variation in the (PAH 8 μm)/160 μm ratio with 160 μm surface brightness is purely driven by the decrease in 160 μm emission relative to TIR emission, as the (PAH 8 μm)/TIR ratio remains constant with TIR surface brightness. In a few exceptions, however, a decline in the PAH 8 μm emission relative to TIR emission is also partly responsible for the observed variations. This reduction of PAH emission may occur if the fraction of starlight from evolved red stars increases as the 160 μm surface brightness decreases. In this scenario, the photons in the illuminating radiation field would have reduced energies, and the peak temperatures attained by PAHs following the absorpiton of single photons would be reduced. Consequently, the PAHs would tend to radiate at longer wavelengths, and the (PAH 8 μm)/160 μm ratio would appear to decrease.

We also noted that the (PAH 8 μm)/160 μm ratio drops within the high surface brightness centre of some galaxies within this sample. A couple of mechanisms could be responsible for this phenomenon. First, AGN may be responsible for inhibiting the PAH 8 μm emission either by changing the ionisation state of the PAHs or by destroying the PAHs. This was also suggested by Smith et al. (2007), who showed that the 7.7 μm PAH spectral feature was suppressed within the centres of SINGS galaxies with low luminosity AGN. Many of the galaxies we observed with suppressed (PAH 8 μm)/160 μm ratios in their centres are objects that are classified as containing AGN, although NGC 3184 is a notable exception. Another possibility is that the (PAH 8 μm)/160 μm ratio drops in regions where a significant fraction of the interstellar radiation field originates from evolved bulge stars. As explained above, PAHs may not be heated as strongly by single photons in such radiation fields, and therefore 7.7 μm emission will be inhibited.

6 CONCLUSION

We have shown that the relation between PAH 8 and 24 μm emission in this sample of spiral galaxies exhibit significant scatter on scales of $\sim$ 2 kpc. In particular, we have shown that the PAH 8 μm emission is relatively weak compared to 24 μm emission in star-forming regions, but the PAH 8 μm emission is relatively strong in the diffuse ISM. In some cases, the (PAH 8 μm)/24 μm ratio may exhibit variations greater than a factor of 2 at a given 24 μm surface brightness. We argue that two mechanisms are responsible for these variations: enhancements in the 24 μm emission relative to PAH emission in regions with very strong radiation fields with high-energy photons and the corresponding reduction of PAH 8 μm emission.

We have also shown that the PAH 8 μm emission is associated with 160 μm emission on scales of $\sim$ 2 kpc within these spiral galaxies and that the (PAH 8 μm)/160 μm ratio appears to be a function of 160 μm surface brightness. The scatter in the relation is only at the 10%-20% level for a given surface brightness, and the intrinsic scatter measured in the relation between the (PAH 8 μm)/160 μm ratio and 160 μm surface brightness is notably lower than for the relation between the (PAH 8 μm)/24 μm ratio and 24 μm surface brightness. While the (PAH 8 μm)/160 μm ratio appears to decrease monotonically with radius in some galaxies, the presence of peaks in the (PAH 8 μm)/160 μm ratio corresponding to large scale structure indicates that surface brightness may be a more important factor, and statistical tests of the best fit lines between the (PAH 8 μm)/160 μm ratio and either 160 μm surface brightness or radius showed that the dependence with 160 μm surface brightness was more significant. The strong correlation between the (PAH 8 μm)/160 μm ratio and 160 μm emission and the results from the comparison of PAH 8 and 24 μm emission suggest that most of the PAHs are located in the diffuse interstellar medium with the dust grains that produce the majority of the 160 μm emission. We therefore suggest that the (PAH 8 μm)/160 μm ratio may be indicative of the intensity of the interstellar radiation field that heats the diffuse interstellar dust in these galaxies.

The results here indicate that PAH emission should be used very cautiously as a tracer of star formation on kiloparsec scales if it should be used at all. Instead, the PAH emission may be more indicative of the distribution of diffuse dust within nearby galaxies, although PAH emission still may be affected by metallicity (Engelbracht et al. 2005; Dale et al. 2005; Calzetti et al. 2007; Engelbracht et al. 2008), and the results here suggest that PAH emission might be inhibited in the diffuse ISM if the radiation field is very high. Follow-up observations with the Herschel Space Observatory and the James Clerk Maxwell Telescope will allow for studying the correlation between PAH and $\sim$ 20 K dust emission on smaller spatial scales in nearby galaxies, thus placing further constraints on the relation between PAHs and cool dust.

ACKNOWLEDGEMENTS

This work was funded by STFC. BTD was supported in part by NSF grant AST04-06883. AL is supported in part by the Spitzer Theory Programs and NSF grant AST 07-07866.

REFERENCES

Allamandola, L. J., Hudgins, D. M., & Sandford, S. A., 1999, ApJ, 511, L115
Bendo, G. J., et al., 2006, ApJ, 652, 283
Calzetti, D., et al., 2005, ApJ, 633, 871
Calzetti, D., et al., 2007, ApJ, 666, 870
Churchwell, E., et al., 2006, ApJ, 649, 759
Dale, D. A., Helou, G., Contursi, A., Silbermann, N. A., & Kolhatkar, S., 2001, ApJ, 549, 215
Dale, D. A., et al., 2005, ApJ, 633, 857
Dale, D. A., et al., 2007, ApJ, 655, 863
de Vaucouleurs, G., de Vaucouleurs, A., Corwin, H. G., Buta, R. J., Paturel, G., & Fouque, P., 1991, Third Reference Catalogue of Bright Galaxies, Springer-Verlag, Berlin
Draine, B. T., et al., 2007, ApJ, 663, 866
Draine, B. T., & Li, A., 2007, ApJ, 657, 810
Engelbracht, C. W., Gordon, K. D., Rieke, G. H., Werner, M. W., Dale, D. A., & Latter, W. B., 2005, ApJ, 628, L29
Engelbracht, C. W., Rieke, G. H., Gordon, K. D., Smith, J.-D. T., Werner, M. W., Moustakas, J., Willmen, C. N. A., & Vanzi, L., 2008, ApJ, 678, 804
Fazio, G. G., et al., 2004, ApJS, 154, 10
Feldmeier, J. J., Ciardullo, R., & Jacoby, G. H., 1997, ApJ, 479, 231
Freedman, W. L., et al., 2001, ApJ, 553, 47
Förster Schreiber, N. M., Roussel, H., Sauvage, M., Charmandaris, V., 2004, A&A, 419, 501
García-Gómez, C., Athanassoula, E., & Barberà, C., 2002, A&A, 389, 68
Gordon, K. D., Engelbracht, C. W., Rieke, G. H., Misselt, K. A., Smith, J.-D. T., Kennicutt, R. C., Jr., 2008, preprint (astro-ph/0804.3223v1)
Gordon, K. D., et al., 2005, PASP, 117, 50
Haas, M., Klaas, U., & Bianchi, S., 2002, A&A, 385, L23
Helou, G., et al., 2004, ApJS, 154, 253
Karachentsev, I. D., Sharina, M. E., & Hutchmeier, W. K., 2000, A&A, 362, 544
Karachentsev, I. D., et al., 2003, A&A, 404, 93
Kauffmann, G., et al., 2003, MNRAS, 346, 1055
Kennicutt, R. C., Jr., et al., 2003, PASP, 115, 928
Kobulnicky, H. A., & Kewley, L. J., 2004, ApJ, 617, 240
Lebouteiller, V., Brandl, B., Bernard-Salas, J., Devost, D., & Houck, J. R., 2007, ApJ, 665, 390
Leonard, D. C., et al., 2002, AJ, 124, 2490
Li, A., & Draine, B. T., 2001, ApJ, 554, 778
Madden, S. C., Galliano, F., Jones, A. P., & Sauvage, M., 2006, A&A, 446, 877
Masters, K. L., 2005, PhD thesis, Cornell University
Mattila, K., Lehtinen, K., & Lemke, D., 1999, A&A, 342, 643
Mei, S., et al., 2007, ApJ, 655, 144
Oey, M. S., et al., 2007, ApJ, 661, 801
Perez-Gonzalez, P. G., et al., 2006, ApJ, 648, 987
Povich, M. S., et al., 2007, ApJ, 660, 346
Prescott, M. K. M., et al., 2007, ApJ, 668, 182
Pilyugin, L. S., & Thuan, T. X., 2005, ApJ, 631, 231
Pilyugin, L. S., Vílchez, J. M., & Contini, T., 2004, A&A, 425, 849
Reach, W. T., et al., 2005, PASP, 117, 978
Regan M. W., et al., 2006, ApJ, 652, 1112
Rho, J., Reach, W. T., Lefloch, B., Fazio, G. G., 2006, ApJ, 643, 965
Roussel, H., Sauvage, M., Vigroux, L., & Bosma, A., 2001, A&A, 372, 427
Rieke, G. H., et al., 2004, ApJS, 154, 25
Searle, L., 1971, ApJ, 168, 327
SINGS Team, 2006, User's Guide, SSC, Pasadena
Sharina, M. E., Karachentsev, I. D., & Tikhonov, N. A., 1996, A&AS, 119, 499
Smith, J. D. T., et al., 2007, ApJ, 656, 770
Smith, N., & Brooks, K. J., 2007, MNRAS, 379, 1279
Spitzer Science Center, 2006, Spitzer Observer's Manual Version 7.1, SSC, Pasadena
Thilker, D. A., et al., 2007, ApJ, 173, 572
Tully, R. B., 1988, Nearby Galaxies Catalogue, Cambridge University Press, Cambridge
van Zee, L., Salzer, J. J., Haynes, M. P., O'Donoghue, A. A., Balonek, T. J., 1998, AJ, 116, 2805
Vila-Costas, M. B., & Edmunds, M. G., 1992, MNRAS 259, 121
Webster, B. L., & Smith, M. G., 1983, MNRAS, 204, 743
Weingartner, J. C., & Draine, B. T., 2001, ApJS, 134, 263
Werner, M. W., et al., 2004, ApJS, 154, 1
Zaritsky, D., Kennicutt, R. C., Jr., & Huchra, J. P., 1994, ApJ, 420, 87